Quaternary Science Reviews 56 (2012) 46–68

Contents lists available at SciVerse ScienceDirect

Quaternary Science Reviews

journal homepage: www.elsevier.com/locate/quascirev

Simulating atmospheric CO_2, ^{13}C and the marine carbon cycle during the Last Glacial–Interglacial cycle: possible role for a deepening of the mean remineralization depth and an increase in the oceanic nutrient inventory

L. Menviel [a,b,c,*], F. Joos [a,b], S.P. Ritz [a,b]

[a] Climate and Environmental Physics, University of Bern, Bern, Switzerland
[b] Oeschger Centre for Climate Change Research, University of Bern, Bern, Switzerland
[c] Climate Change Research Centre, Centre of Excellence, University of New South Wales, Sydney, Australia

ARTICLE INFO

Article history:
Received 16 December 2011
Received in revised form
7 September 2012
Accepted 10 September 2012
Available online 12 October 2012

Keywords:
Glacial–Interglacial cycles
Atmospheric CO_2
Marine carbon cycle
Earth system model of intermediate complexity

ABSTRACT

Using the Earth system model of intermediate complexity Bern3D, we transiently simulate changes in atmospheric CO_2 and climate over the Last Glacial–Interglacial cycle. A third of the glacial–interglacial atmospheric CO_2 change can be explained by relatively well-established forcings such as temperature, salinity, a shallowing and weakening of the Atlantic Meridional Overturning Circulation, iron fertilization of the marine biosphere by aeolian dust input and land carbon inventory changes. A 10% increase in the oceanic phosphate inventory decreases atmospheric CO_2 by 50 ppmv during the glaciation, however due to the long residence time of phosphorus in the ocean and the long time scales of ocean–sediment interactions it only contributes to a 5 ppmv increase between 20 and 0 ka B.P. The enhanced surface nutrient utilisation simulated as a result of a greater oceanic phosphate inventory leads to a good representation of glacial export production and $\delta^{13}CO_2$ changes, lending support to this hypothesis. A deepening of particulate organic matter remineralization can effectively lower pCO_2 during the glaciation, however it leads to a significant increase in deep $[CO_3^{2-}]$ and to changes in export production in poor agreement with paleo-proxies. Finally the parametrization of brine rejection around Antarctica could lead to 10–20 ppmv change in pCO_2, but its timing casts doubt onto its effectiveness in forcing CO_2 variations over the Last Glacial–Interglacial cycle. The results highlight the importance of a transient, 3-dimensional setting for the interpretation of proxy records.

1. Introduction

Analyses of air bubbles trapped in Antarctic ice cores reveal that over the last eight glacial–interglacial (G–IG) cycles, atmospheric CO_2 varied between 172 and 200 ppmv during glacial times and 240 and 300 ppmv during interglacial times (Petit et al., 1999; Siegenthaler et al., 2005; Lüthi et al., 2008). Due to its radiative effect, atmospheric CO_2 provides an important positive feedback to G–IG climatic changes. And, despite its importance, the exact mechanisms leading to G–IG atmospheric CO_2 variations still remain elusive (Archer et al., 2000; Sigman and Boyle, 2000; Kohfeld and Ridgwell, 2009).

Paleo-proxies and model studies suggest that the terrestrial carbon stock was 300–800 GtC lower at the Last Glacial Maximum (LGM) (Curry et al., 1988; Duplessy et al., 1988; Bird et al., 1994; Francois et al., 1998; Beerling, 1999; Kaplan et al., 2002; Joos et al., 2004; Menviel et al., 2008b; Holden et al., 2010a; Ciais et al., 2011). Some authors however argue that terrestrial carbon storage was larger at the LGM than during the more recent pre-industrial period due to carbon storage under continental ice sheets or in permafrost areas (Zeng, 2003; Zimov et al., 2009). This is apparently in conflict with the reconstructed whole ocean lower glacial $\delta^{13}C$ of Dissolved Inorganic Carbon ($\delta^{13}C_{DIC}$) of about 0.3 permil (Curry et al., 1988; Duplessy et al., 1988; Bird et al., 1994).

1.1. Physical mechanisms to lower CO_2

The first mechanism put forward to decrease atmospheric CO_2 during glacial times is greater CO_2 solubility due to lower oceanic temperatures (Bacastow and Maier-Reimer, 1990; Heinze et al., 1991). Model studies estimate that the ~2.5 °C ocean surface glacial cooling is responsible for about 25 ppmv decrease in CO_2

* Corresponding author. Climate Change Research Centre, Centre of Excellence, University of New South Wales, Sydney, Australia.
E-mail address: l.menviel@unsw.edu.au (L. Menviel).

0277-3791/$ – see front matter © 2012 Elsevier Ltd. All rights reserved.
http://dx.doi.org/10.1016/j.quascirev.2012.09.012

(Kohfeld and Ridgwell, 2009, and references therein). This greater solubility is however partially offset (+10–15 ppmv) by the more saline glacial ocean (Broecker and Peng, 1986; Sigman and Boyle, 2000; Ridgwell, 2001; Köhler and Fischer, 2006). Indeed, the build-up of glacial ice sheets lead to a sea level lowering of about 120 m (Fairbanks, 1989; Peltier, 2004) and therefore to a ~3% increase in global salinity.

The analysis of $\delta^{13}C$ in deep ocean sediments (Boyle and Keigwin, 1987; Duplessy et al., 1988; Curry and Oppo, 2005) suggests that the Atlantic Meridional Overturning Circulation (AMOC) was much shallower at the LGM. Some $^{231}Pa/^{230}Th$ (Negre et al., 2010) data and modelling studies (Watkins et al., 2007) indicate that the Glacial North Atlantic Intermediate Water (GNAIW) export was probably weaker than the modern export of North Atlantic Deep Water (NADW). The relative strength of the GNAIW is however still a matter of debate (Yu et al., 1996; Weber et al., 2007; Oliver and Edwards, 2008). On the other side, it is suggested that the Antarctic Bottom Water (AABW) was occupying a greater volume and was penetrating more northward into the Atlantic (Lund et al., 2011) at the LGM. These circulation changes could have an impact on atmospheric CO_2.

Deep waters that upwell in Antarctica have a high CO_2 content and are a source of CO_2 to the atmosphere. Paleo-proxy (Francois et al., 1997; Spero and Lea, 2002; Anderson et al., 2009; Burke and Robinson, 2012; Schmitt et al., 2012) and model studies (Tschumi et al., 2011) suggest that a change in Southern Ocean ventilation contributed to the G–IG CO_2 rise. An initial deglacial CO_2 rise caused by enhanced Southern Ocean ventilation would be consistent with a drop in atmospheric radiocarbon (Reimer et al., 2009) and an opal peak in Southern Ocean sediments (Anderson et al., 2009). An increase in Southern Ocean sea ice extent or a greater stratification in the Southern Ocean during glacial times could decrease the CO_2 leakage to the atmosphere by reducing air–sea gas exchange (Francois et al., 1997; Toggweiler, 1999; Sigman and Boyle, 2000). Gildor and Tziperman (2001) propose an increase in Southern Ocean stratification due to a cooling of the NADW during the glaciation. However, a study of LGM climate as simulated by state of the art Atmosphere–Ocean General Circulation Models (AOGCMs) shows no increase in Southern Ocean stratification due to a cooling of the NADW (Weber et al., 2007). Paillard and Parrenin (2004) suggest that during the glaciation as temperature dropped and the sea level lowered the formation of brines was enhanced. Brines formed in the Weddell and Ross Seas sink along the continental shelf to depth hardly mixing with surrounding waters, thus leading to the formation of very dense AABW and to an increase in ocean stratification. This process however ceased at the peak of the glaciation as the main regions of AABW formation, the Ross and Weddell Seas were covered by a grounded ice sheet and the formation of brines was pushed to the open ocean.

Finally, Sigman and Boyle (2000) and Toggweiler et al. (2006) propose that an equatorward shift of the Southern Hemispheric westerlies would lead to a reduced upwelling of CO_2-rich waters in the Southern Ocean. But, LGM southern hemispheric westerly winds as simulated in AOGCMs do not display a consistent weakening nor a significant latitudinal shift (Menviel et al., 2008a; Rojas et al., 2009) and the associated response in CO_2 was found to be small (Tschumi et al., 2008; Menviel et al., 2008a).

In addition, while greater Southern Ocean sea ice coverage has a significant impact on atmospheric CO_2 in box models (Stephens and Keeling, 2000; Gildor and Tziperman, 2001; Gildor et al., 2002; Köhler et al., 2005), the effect is very small in AOGCMs (Archer et al., 2003; Kurahashi-Nakamura et al., 2007; Chikamoto et al., 2012).

1.2. Biological mechanisms to lower CO_2

Analyses of Antarctic ice core records revealed that iron-rich dust deposition was much greater during glacial than interglacial times (Petit et al., 1999; Wolff et al., 2006; Lambert et al., 2008). As iron is an essential limiting nutrient for marine productivity, Martin (1990) suggest that a greater input of aeolian iron to the ocean during glacial times could increase the efficiency of the biological pump thereby lowering atmospheric CO_2. While iron fertilization has a significant impact on CO_2 in box models (up to 40 ppmv) (Joos et al., 1991; Lefevre and Watson, 1999; Watson et al., 2000), its effect in 3-dimensional models is more modest (8–15 ppmv) (Bopp et al., 2003; Parekh et al., 2006a, 2006b).

Broecker (1982) first proposed that as the sea level dropped during the glaciation and marine continental shelves were exposed, the ocean phosphate inventory would increase and stimulate export production so as to decrease atmospheric CO_2. Weathering of freshly exposed continental margin sediments, which comprises the bulk of reactive phosphorus would add phosphate to the open ocean (Guidry and Mackenzie, 2003). In addition, removing the continental margin sink of phosphate would further increase the oceanic phosphate content (Filippelli, 1997). Marine ocean sediment cores from the Southern Ocean and the equatorial Pacific Ocean show greater dissolved phosphate inventory during glacial than interglacial times (Filippelli et al., 2007). Tamburini and Föllmi (2009) further suggest that the oceanic phosphate inventory could have been 17–40% greater during glacial than interglacial times. Box models and models of intermediate complexity have shown that atmospheric CO_2 could lower by 30–60 ppmv when the oceanic phosphate content increases by 30% (Heinze et al., 1991; Sigman et al., 1998; Tschumi et al., 2011).

Finally, biological activity increases with temperature in marine and terrestrial ecosystems (Eppley, 1972; Edwards, 1975; Laws et al., 2000). Due to nutrient limitations, the new marine production is not generally limited by temperature (Steinacher et al., 2010). However, Particulate Organic Matter (POM) exported from the surface is gradually remineralized in the water column by bacteria. A cooling of the ocean during glacial times could have an impact on the metabolic rate of these bacteria and therefore slow down the rate of POM remineralization and deepen the remineralization depth. An increase in the remineralization depth could also be obtained by a faster sinking rate of POM. In their study Biermann and Engel (2010) show that under low CO_2 coccolithophore $CaCO_3$ shells are less porous and fragile than under high CO_2. $CaCO_3$-POM aggregates thus sink twice as fast when the atmospheric CO_2 content is equal to 180 ppmv than when it amounts 380 ppmv. The lower glacial CO_2 could indirectly act on the sinking rate of POM and lead to a greater flux of DIC to the deep ocean, thus providing a positive feedback to the CO_2 lowering. Using a model of intermediate complexity (GENIE-1) Matsumoto (2007) obtain a 30 ppmv CO_2 reduction in response to a 5 °C global cooling. Kwon et al. (2009) confirm the possible high sensitivity of CO_2 to changes in the remineralization depth by simulating 10–27 ppmv CO_2 reduction when the depth above which 63% of the sinking carbon is remineralized deepens by 24 m in a 3-dimensional model. Finally, using a marine ecosystem model (PISCES) Schneider et al. (2008) show that by improving the efficiency of the POM transfer to depth a significantly lower atmospheric CO_2 is obtained. All of these experiments are however performed in a very idealised setting and without a sediment model.

Unravelling the mysteries of G–IG atmospheric CO_2 variations relies on modelling experiments and proxy data. Sensitivity studies of the marine carbon cycle to climatic and biogeochemical changes have been performed with AOGCMs coupled to a carbon cycle model, earth system models of intermediate complexity and box models.

Due to high computing times, the sensitivity of carbon cycle to different factors has been assessed with AOGCMs by highly idealised experiments performed under constant boundary conditions. While there is a consensus that the G–IG change in atmospheric CO_2 can only be explained by a combination of factors, only few modelling studies combined different hypotheses in a 3-dimensional setting (Tagliabue et al., 2009; de Boer et al., 2010). Transient experiments of the Last Glacial cycle were only performed so far with 2-dimensional models (Ridgwell, 2001; Brovkin et al., 2012). In their study, Brovkin et al. (2012) obtain an 80 ppmv CO_2 decrease due to increased CO_2 solubility as a result of lower temperature, iron fertilization, $CaCO_3$ precipitation shift from the coastal area to the deep ocean as well as changes in weathering. On the other hand, Ridgwell (2001) simulates a ~50 ppmv CO_2 decrease with the same mechanisms but without including changes in weathering.

The purpose of this study is to describe the spatio-temporal co-evolution of a range of oceanographic tracers and of atmospheric CO_2 over the last 125 ka in response to a set of proposed physical and biogeochemical forcings applied in the Bern3D climate–carbon model of intermediate complexity. We present the first fully transient climate–carbon cycle simulations through an entire glacial–interglacial cycle with a dynamic model that resolves the three dimensional structure of ocean circulation, ocean biogeochemistry, and marine sediments. Another novel feature is that the amplification by sediment interactions of the atmospheric CO_2 response to changes in remineralization depth of organic material is quantified. Forcings include reconstructed changes in (i) orbital parameters, radiative forcing by (ii) greenhouse gases and (iii) ice sheet albedo, (iv) freshwater fluxes into the North Atlantic from ice sheet volume changes, (v) brine rejection along the Antarctic shelves, (vi) aeolian iron deposition, (vii) remineralization depth of particulate organic matter, (viii) oceans phosphate inventory and (ix) land carbon storage. These forcings are applied in combination as well as in factorial experiments to document their combined or individual physical and biogeochemical impacts. Results of these experiments are compared to available paleo-proxies, notably $\delta^{13}CO_2$, deep $\delta^{13}C_{DIC}$ and deep $[CO_3^{2-}]$. Given the complexity of the problem, the limited knowledge on the evolution of various forcings as well as uncertainties in model and proxy data, we do not attempt to provide the ultimate attribution of mechanisms to G–IG CO_2 changes nor do we investigate individual, previously proposed, mechanisms in detail. Rather, the goal is to document forcing–response relationships on multi-millennial time scales in a transient, dynamic and 3-dimensional setting.

2. Model and experimental set-up

2.1. Bern3D ocean carbon cycle model

The Bern3D model represents atmospheric, terrestrial, oceanic and sedimentary reservoirs. The physical ocean model, with a horizontal resolution of 36 × 36 grid boxes and 32 unevenly spaced layers, is a three-dimensional frictional geostrophic balance ocean model (Müller et al., 2006), which has been further developed from the three-dimensional rigid-lid ocean model of Edwards et al. (1998) as updated by Edwards and Marsh (2005). The atmospheric model is an Energy Balance Model (EBM), which details and coupling to the physical ocean model are described in Ritz et al. (2011). The single-layer energy balance includes a hydrological cycle and has the same temporal and horizontal resolutions as the ocean model. The time-varying incoming insolation is calculated as a function of latitude using the algorithm of Berger (1978). The climate sensitivity of the model for a doubling of the atmospheric CO_2 content is 3 °C (Ritz et al., 2011). The marine biogeochemical cycle model is a 3-dimensional global model of the oceanic carbon cycle, fully coupled to the physical ocean model (Parekh et al., 2008; Tschumi et al., 2008). The prognostic state variables considered in the model are dissolved inorganic carbon (DIC), total alkalinity, ^{13}C, ^{14}C, phosphate (PO_4^{3-}), organic products, oxygen, silica and iron. New production is a function of temperature, light, phosphate and iron following Doney et al. (1996). The competition between opal and calcite producers is modelled following the formulations of the HAMOCC5 model of Maier-Reimer et al. (2005). ^{13}C fractionation occurs during marine photosynthesis (Freeman and Hayes, 1992) and the formation of calcium carbonate (Mook, 1988). The air–sea gas exchange is implemented following OCMIP-2 (Najjar et al., 1999; Orr and Najjar, 1999), but applying a linear relationship between wind speed and gas exchange rate (Krakauer et al., 2006) and a lower global average transfer rate following (Müller et al., 2008). Air–sea ^{13}C exchange is subject to kinetic fractionation (Siegenthaler and Muennich, 1981). ^{14}C is represented as a fractionation-corrected concentration. The sedimentary component represents sediment formation, redissolution, remineralization as well as sediment diagenesis in the top 10 cm beneath the seafloor (Heinze et al., 1999; Gehlen et al., 2006). The accumulation of opal, $CaCO_3$ and organic matter is calculated on the basis of a set of dynamical equations for the sediment diagenesis process (Tschumi et al., 2011). Here, the land carbon is represented by the 4-boxes model of Siegenthaler and Oeschger (1987).

A similar set-up of the model was used in Menviel and Joos (2012) and Roth and Joos (2012), while Tschumi et al. (2011) discuss in details the pre-industrial performance of the ocean–sediment components. The coupling of the ocean–sediment modules to the EBM leads to slight changes in ocean circulation and tracer distribution. A description of the initialisation of the model and of the pre-industrial performances with the EBM can be found in Ritz et al. (2011). The modelled temperature, salinity and phosphate distributions obtained in our pre-industrial run are similar to the ones shown in Ritz et al. (2011), and are thus in reasonable agreement with observations. Under pre-industrial conditions, the simulated export fluxes amount to 13.5 GtC/yr for organic matter, 1.2 GtC for $CaCO_3$ and 107 Tmol Si/yr for opal, in agreement with other modelling studies (Jin et al., 2006).

2.2. Experiments performed

From the pre-industrial control state (Menviel and Joos, 2012), we perform a series of transient experiments from 125 to 0 ka B.P. (Table 1). An experiment ran under constant Eemian (125 ka B.P.) conditions is also used as control. As can be seen in Ritz et al. (2011), the Bern3D simulates similar conditions at the Eemian and the pre-industrial so that the total change in atmospheric CO_2 simulated by the control run is 2 ppmv.

All the experiments are forced with time-varying changes in insolation (Berger, 1978), ice sheet extent as well as radiative changes due to the varying atmospheric CO_2 (Lüthi et al., 2008) and CH_4 content (Loulergue et al., 2008). The ice sheet extent forcing uses the LGM ice sheet mask from Peltier (1994), which is scaled on the global ice volume (benthic $\delta^{18}O$ stack (Lisiecki and Raymo, 2005)). Changes in the albedo, salinity and heat flux associated with the ice sheet build-up/melting are also taken into account (Ritz et al., 2011). The set-up in the Bern3D allows us to force the climate module with the observed atmospheric CO_2 changes, while computing interactively the atmospheric CO_2 changes in the biogeochemical module. During the transient experiments, the riverine flux of the different tracers is kept constant at pre-industrial values. Large uncertainties remain as to the evolution of the wind field during glacial–interglacial cycles. As the EBM does not interactively compute the wind field, we continuously force the

Table 1
Main experiments performed in this study. (–) means constant pre-industrial forcing, (X) means a variable forcing as described in Section 2.2. Physics include orbital, CH_4 radiative forcing as well as albedo and freshwater forcing. CO_2 F indicates that the climate part of the model is forced with the ice core atmospheric CO_2 record, while CO_2 I indicates that the CO_2 calculated by the biochemical part also forces the climate part of the model. Remi. X indicates that changes in the remineralization depth were applied. Land X means that the fluxes in between the different land carbon reservoirs and the atmosphere are varied so as to simulate changes in the land carbon stock.

Experiment	Physics	CO_2	Iron input	Land	Remi.	Brine param.	P inventory
$S1_{(Rem,P)}$ FC	X	I	X	X	X	–	X
$S2_{(Rem,Br)}$ FC	X	I	X	X	X	X	–
$S1_{(Rem,P)}$	X	F	X	X	X	–	X
$S2_{(Rem,Br)}$	X	F	X	X	X	X	–
$S3_{(Br,P)}$	X	F	X	X	–	X	X
REM	X	F	X	–	X	–	–
BR	X	F	X	–	–	X	–
PO	X	F	X	–	–	–	X
VG	X	F	X	X	–	–	–
FE	X	F	X	–	–	–	–
OC	X	F	–	–	–	–	–
TS	X*	F	–	–	–	–	–

* In experiment TS a different freshwater forcing is applied compared to the other experiments.

model with present-day estimates of the windstress as derived from the NCEP reanalysis (Müller et al., 2006).

Freshwater is extracted uniformly over the ocean following the global ice volume proxy, the benthic $\delta^{18}O$ stack (Lisiecki and Raymo, 2005), to simulate ice sheet build-up (Ritz et al., 2011). As the freshwater forcing resulting from melting ice sheets inferred from the benthic $\delta^{18}O$ stack does not lead to a good representation of some of the abrupt millennial-scale variability, the model is forced with a more idealised freshwater time series in all experiments but TS. In this forcing, freshwater is added in the North Atlantic (Fig. 1b) and is designed so as to match the millennial-scale events observed in the Iberian margin benthic $\delta^{13}C$ record of Martrat et al. (2007) for the period 125–20 ka B.P and the ϵNd record of Piotrowski et al. (2008) for the period 90–20 ka B.P. During the deglaciation, the freshwater forcing in the North Atlantic follows Heinrich Event 1 and the Younger Dryas as observed in the $^{231}Pa/^{230}Th$ record of McManus et al. (2004). The magnitude of the fluxes is set to obtain a decrease of 120 m in sea level (Fig. 1d) as well as 1 in global salinity from 125 to 20 ka B.P.

In all but experiments TS and OC, the model is forced with a varying dust input. The LGM dust input distribution is taken from Mahowald et al. (2006) and the pre-industrial field is based on Luo et al. (2003). The aeolian dust deposition history is computed by linearly interpolating the LGM and the pre-industrial fields using the reconstructed iron flux evolution from the EPICA Dome C ice core (Wolff et al., 2006) (Fig. 1e). To explore the uncertainties associated with the LGM dust input distribution, two additional experiments are performed. In one experiment (FEx2) the LGM iron flux is doubled and in the other (FEsP) the LGM iron flux to the South Pacific is quadrupled.

We then test the impact of an increase in the oceanic phosphate inventory on the marine carbon cycle (experiments PO, $S1_{(Rem,P)}$ and $S3_{(Br,P)}$). It is hypothesized that the oceanic phosphate inventory increases as the continental margin is exposed following the sea level drop. We thus increase the river influx of phosphate by up to 20% at the LGM. The anomalies in the phosphate flux from land to ocean are prescribed to be proportional to the sea level change (Fig. 1d). The timing of the increase is thus based on the benthic $\delta^{18}O$ stack of Lisiecki and Raymo (2005).

In a next step, both the remineralization rates of particulate (POM) and dissolved organic matter (DOM) are changed. In the Bern3D the downward flux of POM below the euphotic zone at a depth z is defined by:

$$F(z) = F(z_0)\cdot(z/z_0)^{-b} \quad (1)$$

(Martin et al., 1987), where z_0 represents the base of the euphotic zone and b is a dimensionless scaling factor controlling the efficiency of POM transfer to depth. As in most carbon cycle models, b is constant and set at 0.9. However, observations have shown that, depending on the region, community structure and mineral ballast, the scaling factor b varies substantially (from 0.7 to 1.3) in the modern ocean (e.g. Berelson, 2001; Klaas and Archer, 2002; Buesseler et al., 2007; Martin et al., 2011). Remineralization rates of POM are changed differently depending on the latitude. In the high northern (35°N–90°N) and southern latitudes (35°S–90°S), b was varied from 0.9 (125 ka B.P.) to 0.8255 (LGM), which corresponds to ~26 m increase in the depth above which 63% of the POM is remineralized (experiments REM, $S1_{(Rem,P)}$ and $S2_{(Rem,Br)}$). At low latitudes (35°S–35°N) b was varied from 0.9 (125 ka B.P.) to 0.86 (LGM), which is equivalent to a 12 m deepening of the POM remineralization. The variations of b are scaled on the zonally averaged thermocline temperature simulated by the Bern3D at respectively high northern, high southern and low latitudes (Fig. 1c).

Ocean temperature changes could also have an impact on the remineralization of DOM. Modelling studies estimated the life time of semi-labile DOM at about 0.5–1 year (Six and Maier-Reimer, 1996; Yamanaka and Tajika, 1996). Recent studies suggest that a significant portion of DOM is degraded by bacteria and is thus temperature dependent (Bendtsen et al., 2002; Middelboe and Lundsgaard, 2003; Carlson et al., 2010). The bacteria growth rate in an oceanic environment has been shown to roughly double for a 10 °C increase in temperature ($Q_{10} = 2$). This would equate to increase the life time of DOM in our experiments from 0.5 year at the Eemian (125 ka B.P.) to 0.705 year at the LGM (experiments REM, $S1_{(Rem,P)}$ and $S2_{(Rem,Br)}$). This change in DOM life time is scaled on the globally averaged thermocline temperature simulated by the Bern3D in experiment OC.

The influence on the marine carbon cycle of the formation of very dense AABW during the glaciation through the sinking of brines is also studied (experiments BR, $S2_{(Rem,Br)}$ and $S3_{(Br,P)}$). Through a similar method as the one described in Bouttes et al. (2010), a portion of the salt and geochemical variables (DIC, $DI^{13}C$, ALK, PO_4, Si) rejected during sea ice formation is directly transported to the bottom most cell of the model. This method is applied in the Southern Ocean in the area encompassing the Ross and Weddell Seas (180–360°E). The fraction (*frac*) of the salt and geochemical variables transported to depth is set to vary between 0 and 0.4 in agreement with previous study (Bouttes et al., 2011), and its evolution depends on the climate, the sea level and the extent of the Antarctic ice sheet (Appendix A). *frac* is high when the sea level is relatively low and the Antarctic ice sheet extent is medium (88 ka B.P., 50 ka B.P. and 37 ka B.P.) whereas *frac* is low during interglacial times as well as when the Antarctic ice sheet reaches its maximum extent (21–19 ka B.P.) (Fig. 1d) (Pollard and DeConto, 2009). As the Antarctic ice sheet reaches its maximum extent, the Ross and Weddell Seas are covered by grounded ice and the formation of AABW through the sinking of brines is halted (Paillard and Parrenin, 2004).

The land carbon reservoir was most likely reduced at the LGM compared to pre-industrial times due to globally drier and colder conditions as well as an extended continental ice sheet (Curry et al., 1988; Duplessy et al., 1988; Bird et al., 1994; Francois et al., 1998; Beerling, 1999; Kaplan et al., 2002). Transient experiments of the last deglaciation performed with vegetation models such as

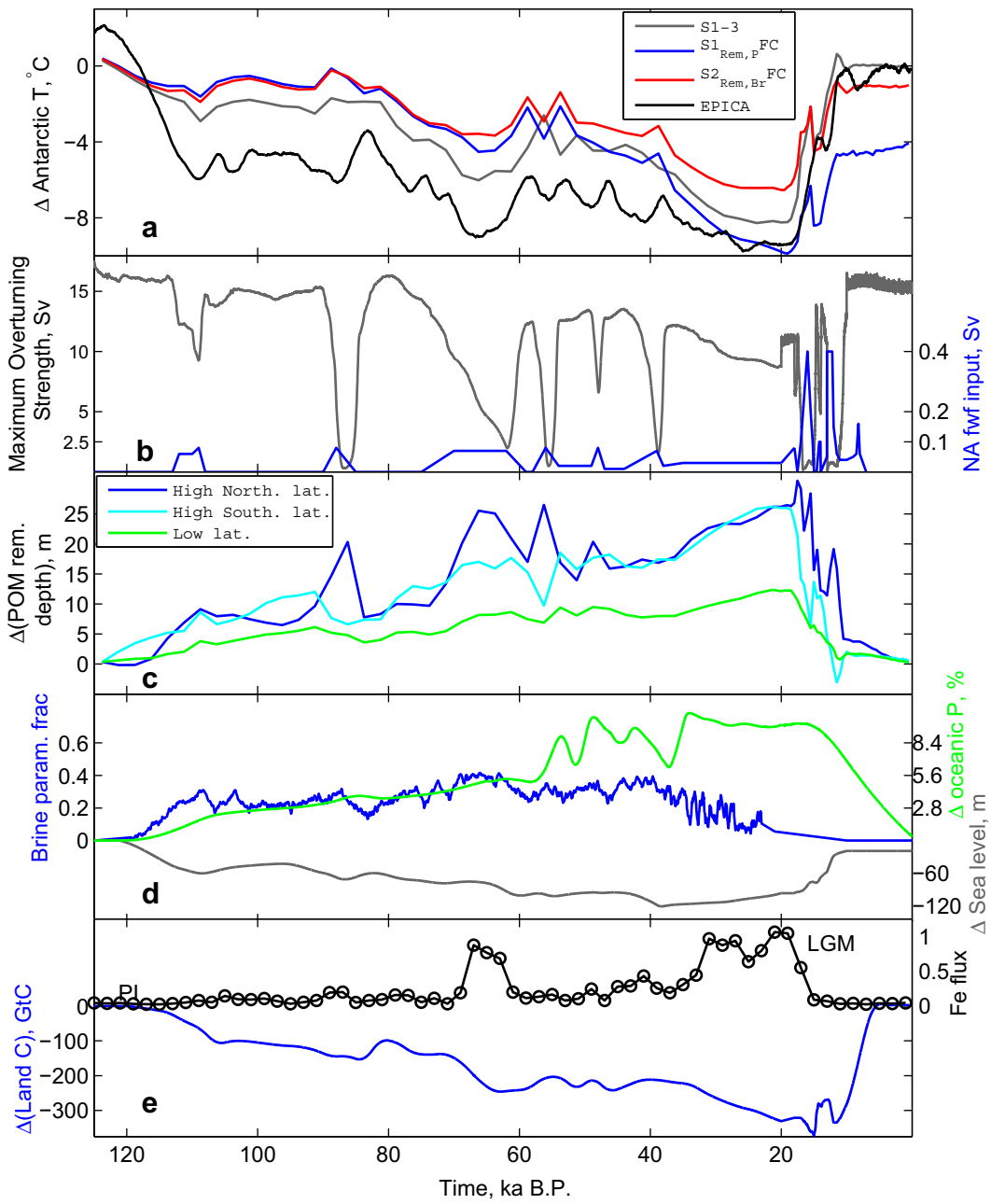

Fig. 1. Main physical variables and forcings: Time series of (a) simulated air temperature anomaly (°C) averaged over Antarctica for simulations S1–3 (grey), $S1_{Rem,P}$ FC (blue), $S2_{Rem,Br}$ FC (red) and as derived from EPICA Dome C ice core (Jouzel et al., 2007) (black); (b) maximum overturning strength (Sv) in the North Atlantic as simulated in experiment OC (grey) and freshwater forcing into the North Atlantic (Sv, blue); (c) changes in POM remineralization depth (m) for the high northern latitudes (dark blue), the high southern latitudes (light blue) and the low latitude (green); (d) brine parametrization factor *frac* (blue), simulated changes in oceanic P inventory (%) (green) and prescribed change in sea level (m, grey); (e) normalised aeolian iron input based on the EPICA Dome C ice core data (Wolff et al., 2006) (black) and change in land carbon inventory (GtC, blue). (For interpretation of the references to colour in this figure legend, the reader is referred to the web version of this article.)

LPJ-DGVM (Kaplan et al., 2002; Joos et al., 2004) or VECODE (Menviel et al., 2011) suggest a terrestrial carbon reduction of about 600–800 GtC at the LGM. On the other hand, exposed continental shelves due to the lower glacial sea level could store about 230–250 GtC at the LGM (Joos et al., 2004; Montenegro et al., 2006). In addition, recent measurements of ^{18}O in atmospheric oxygen suggest a land carbon G–IG change of ~350 GtC (Ciais et al., 2011). Transient changes in land carbon are taken into account by prescribing the fluxes between the different land carbon reservoirs and the atmosphere. A highly idealised land carbon change scenario is applied in which the land carbon release from 125 to 20 ka B.P. amounts to 340 GtC (experiments VE and ALL) and is proportional to the simulated global air temperature anomaly (Fig. 1e). During the deglaciation, the land carbon uptake also amounts to 340 GtC and follows an estimate from a transient experiment performed with LOVECLIM (Menviel et al., 2011) for the first 10 ka after which the mass balance estimate of Elsig et al. (2009) is used (Menviel and Joos, 2012).

Finally, coral reef growth and other forms of shallow-water carbonate deposition most likely contributed significantly to the CO_2 rise during the Holocene (Ridgwell et al., 2003; Kleinen et al., 2010). This process is not represented in the ocean–sediment

module of the Bern3D. Here, shallow-water carbonate deposition is taken into account by removing uniformly from the surface ocean alkalinity and DIC in a 2:1 ratio and at a rate following the deposition scenario suggested by Vecsei and Berger (2004) (Menviel and Joos, 2012). It is noted that potential earlier changes in shallow water carbonate deposition and dissolution are not taken into account.

We apply the forcings described above in different combinations to deconvolute their individual and combined effects on atmospheric CO_2 and on the marine carbon cycle (Table 1, Appendix B). We also perform the fully coupled version of experiments $S1_{(Rem,P)}$ and $S2_{(Rem,Br)}$: in experiments $S1_{(Rem,P)}$ FC and $S2_{(Rem,Br)}$ FC the atmospheric CO_2 calculated by the biochemical part of the model is also used to force the climate part of the model.

3. Climate evolution during the glaciation and at the Last Glacial Maximum

To be able to reproduce the biogeochemical changes during glacial–interglacial cycles, we first need to simulate in a reasonable way the climate evolution. We thus first look at the climate evolution during a transient experiment from the Eemian (125 ka B.P.) to the LGM (20 ka B.P.) forced with changes in orbital parameters, greenhouse gases radiative forcing, continental ice sheet evolution and its associated freshwater forcing (experiment OC) (Fig. 1b).

During the glaciation, the global-mean annual atmospheric surface temperature and SST decrease by respectively 4.5 °C and 2.6 °C, while the globally-averaged salinity increases by 1.1. Due to the general cooling of the Earth's atmosphere under glacial conditions, the global-mean precipitation decreases by about 10%.

As seen in Fig. 2a, given the coarse resolution of the model and uncertainties in SST reconstructions, the modelled SST anomalies at the LGM (set here at 20 ka B.P.) relative to pre-industrial times are in reasonable agreement with the annual mean MARGO reconstruction (Waelbroeck et al., 2009). The LGM SST is up to 5 °C lower in the Southern Ocean between 40°S and 60°S and in the North Atlantic, while the cooling amounts to about 1–2 °C at low latitudes. The main model-data discrepancies occur in the tropical area of the Southern Hemisphere, where the model simulates cooler conditions than the ones inferred by paleo-proxies. In addition, a few sediment cores from the Greenland Iceland Norwegian (GIN) seas suggest warmer conditions there during the LGM, a feature that is not displayed by the Bern3D. However, even state of the art

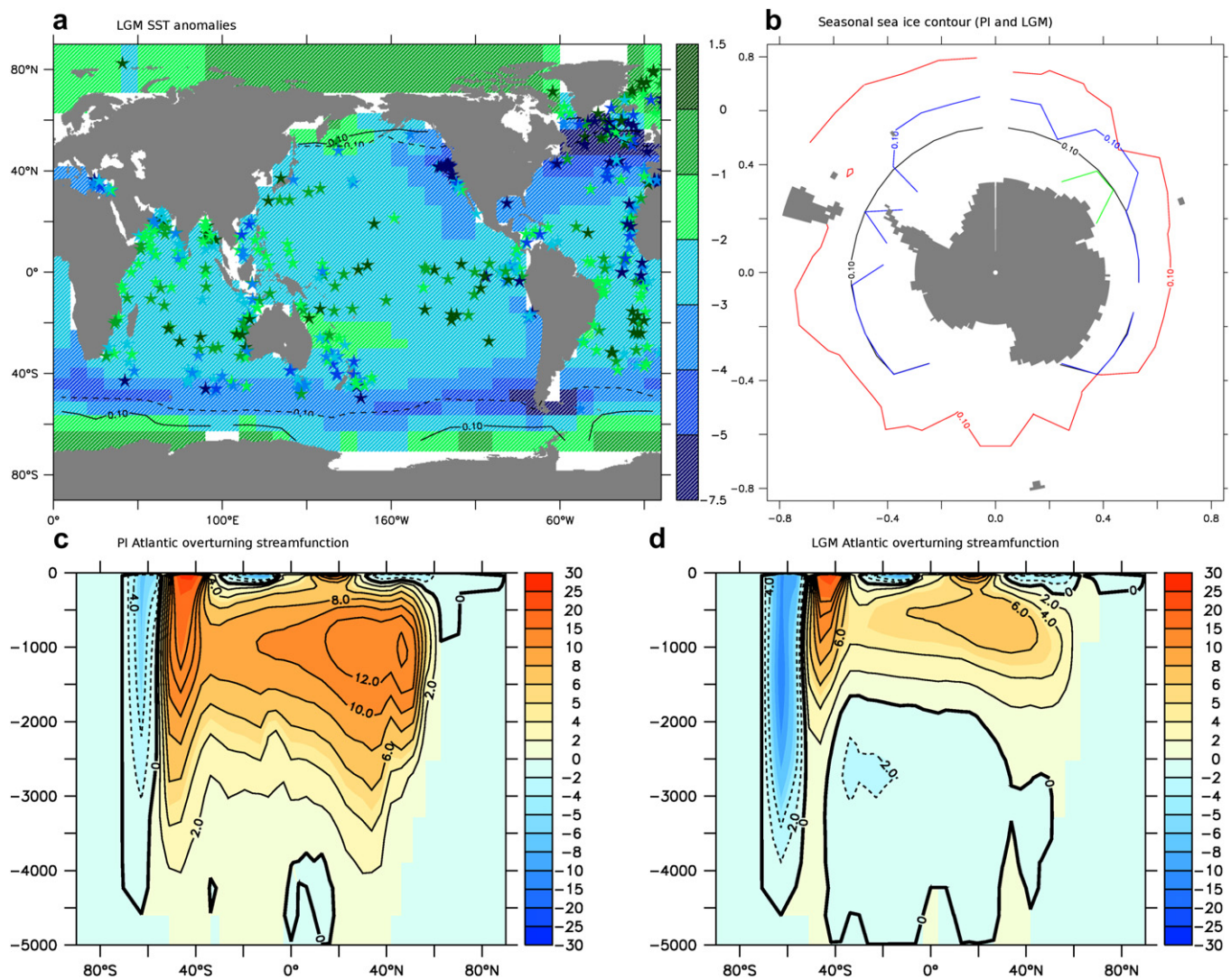

Fig. 2. (a) Annual-mean simulated SST anomalies at the Last Glacial Maximum (LGM) relative to 0 ka B.P. compared to the annual mean MARGO reconstruction (Waelbroeck et al., 2009). Overlaid is the 0.1 m annual sea ice edge as simulated for pre-industrial times (solid line) and at the LGM (dashed line). (b) 0.1 m sea ice edge as simulated for pre-industrial times for DJF (green) and JJA (blue) as well as for the LGM for DJF (black) and JJA (red). (c) Overturning streamfunction (Sv) averaged over the Atlantic basin for the pre-industrial control state. (d) Same as (c) for the simulated LGM state. (For interpretation of the references to colour in this figure legend, the reader is referred to the web version of this article.)

climate models tend to simulate cooler conditions in the south tropical area and warmer conditions in the GIN seas than the one showed in the MARGO reconstruction (Waelbroeck et al., 2009).

The high latitude cooling leads to an equatorward expansion of the sea ice in the Southern Ocean, the North Atlantic and the North Pacific. The annual sea ice edge shifts by 7° equatorward in the Southern Ocean in relative agreement with paleoreconstructions (Gersonde et al., 2005; Allen et al., 2011). During glacial times, the simulated Austral winter sea ice edge (Fig. 2b, red line) expands northward significantly in the Southwest Pacific and the Southwest Atlantic compared to pre-industrial times (black line). Almost no sea ice is simulated in the Southern Ocean during Austral summer in the pre-industrial run (Fig. 2b, green line), whereas the glacial Austral summer sea ice edge (blue line) reaches as far as the pre-industrial Austral winter sea ice edge (black line). In the North Atlantic both model and paleo-proxies show an extension of the sea ice edge south of Iceland and down to St Pierre et Miquelon (de Vernal and Hillaire-Marcel, 2000; Pflaumann et al., 2003; de Vernal et al., 2005) (Fig. 2a).

The evolution of the modelled Antarctic air temperature anomaly is shown in Fig. 1a for experiments S1–3 (grey), $S1_{Rem,P}$ FC (blue) and $S2_{Rem,Br}$ FC (red). The magnitude of the temperature change and its timing are in relative agreement with the air temperature reconstructed from EPICA ice core (Jouzel et al., 2007). However, the cooling simulated at about 110 ka B.P. is much smaller than the one inferred from the proxy. This discrepancy is most likely due to the simplified physics of the model used and the lack of an interactive ice sheet model (Holden et al., 2010b).

The division between NADW and AABW in the Atlantic basin shoals to about 2000 m compared to about 3500 m at 125 and 0 ka B.P. (Fig. 2b and c). Such a shallower NADW at the LGM is in agreement with $\delta^{13}C$ and $\delta^{18}O$ data (Boyle and Keigwin, 1987; Duplessy et al., 1988; Curry and Oppo, 2005; Lund et al., 2011). In addition, the maximum overturning in the North Atlantic amounts to 9 Sv at 20 ka B.P. compared to 16.5 Sv at 0 ka B.P. (Fig. 1b), while the export of AABW at 30° is ~4 Sv higher at 20 ka B.P.

While not perfect, the simulated climate evolution during the glaciation provides a reasonable framework to study the atmospheric and marine carbon cycle changes from 125 ka B.P. to pre-industrial times.

4. Simulating atmospheric CO_2 changes during the Last Glacial–Interglacial cycle

4.1. Atmospheric CO_2 response to a combination of forcings

The experiments S1–3 are forced with changes in orbital parameters, greenhouse gases radiative forcing, continental ice sheet evolution and its associated freshwater forcing, aeolian iron input and land carbon changes. In addition two of the following forcings are used in combination: change in remineralization depth ($S1_{(Rem,P)}$ and $S2_{(Rem,Br)}$), brine rejection parametrization ($S2_{(Rem,Br)}$ and $S3_{(Br,P)}$) and increase in oceanic phosphate inventory ($S1_{(Rem,P)}$ and $S3_{(Br,P)}$).

As seen in Fig. 3a, during the glaciation atmospheric CO_2 decreases by 112 ppmv in experiment $S1_{(Rem,P)}$, 72 ppmv in

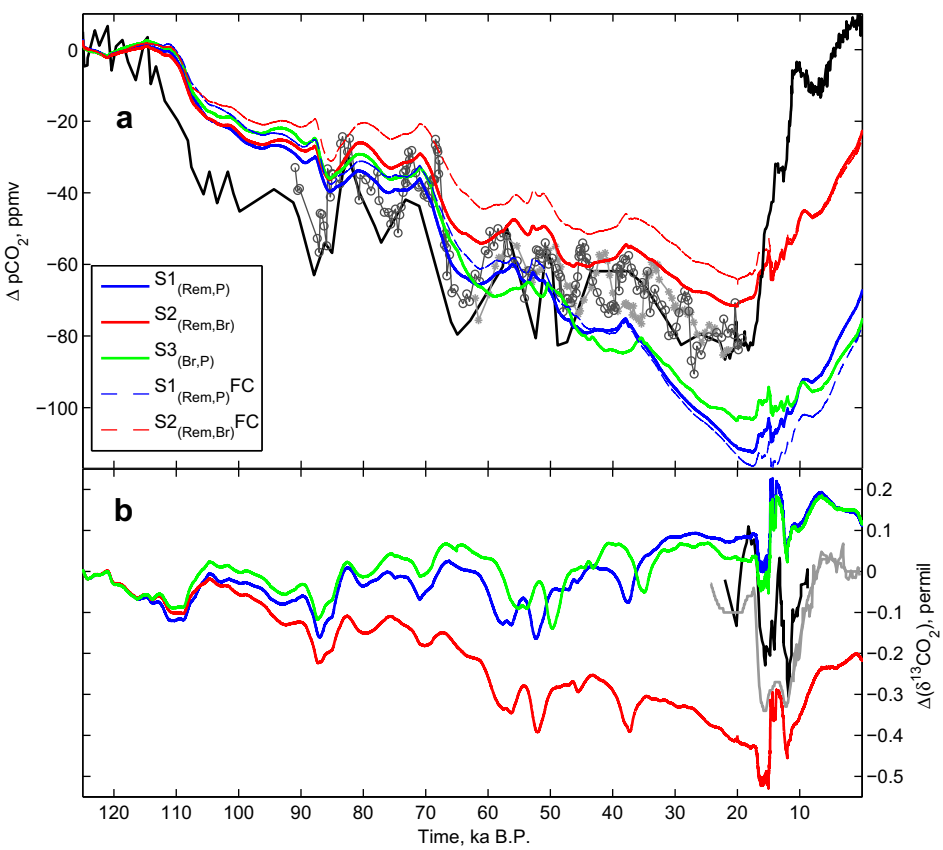

Fig. 3. Time series of (a) atmospheric CO_2 anomalies (ppmv) and (b) atmospheric $\delta^{13}CO_2$ anomalies (permil) for simulations $S1_{(Rem,P)}$ (blue), $S2_{(Rem,Br)}$ (red) and $S3_{(Br,P)}$ (green). The fully coupled simulations $S1_{(Rem,P)}$ FC (dashed blue) and $S2_{(Rem,Br)}$ FC (dashed red) are also shown. Simulations S1–3 are compared to (a) the atmospheric CO_2 record from Vostok ice core (black) (Petit et al., 1999; Lüthi et al., 2008), Taylor Dome ice core (light grey, stars) (Indermühle et al., 2000) and Byrd ice core (dark grey, circles) (Ahn and Brook, 2007, 2008); (b) the atmospheric $\delta^{13}CO_2$ record from EPICA Dome C ice core (Lourantou et al., 2010) (black) and the combination of EPICA Dome C and Talos Dome ice core data (Schmitt et al., 2012) (grey). (For interpretation of the references to colour in this figure legend, the reader is referred to the web version of this article.)

experiment $S2_{(Rem,Br)}$ and 102 ppmv in experiment $S3_{(Br,P)}$. The 3 experiments start to differ significantly at about 65 ka B.P., when pCO_2 is about 10 ppmv lower in experiments $S1_{(Rem,P)}$ and $S3_{(Br,P)}$ than in $S2_{(Rem,Br)}$. The difference between the experiments increases even more at about 37 ka B.P. as the increase in phosphate inventory imposed in $S1_{(Rem,P)}$ and $S3_{(Br,P)}$, but not in $S2_{(Rem,Br)}$ is very effective in reducing atmospheric CO_2. The 3 experiments underestimate the pCO_2 decrease at 110 ka B.P. One reason for this discrepancy is that our model does not simulate properly the timing of the cooling during the deglaciation (Fig. 1a). Experiment $S1_{(Rem,P)}$ FC follows closely experiment $S1_{(Rem,P)}$, while the underestimation of the simulated atmospheric CO_2 in $S2_{(Rem,Br)}$ leads to an even smaller glacial pCO_2 decrease (−65 ppmv) (Fig. 3a).

In addition, despite the strong changes in the simulated AMOC strength, our model does not reproduce the pCO_2 variability associated with millennial-scale variability during the glaciation. This could be due to several reasons: the brine parametrization and land carbon forcings do not include any millennial-scale variability; the aeolian iron input and freshwater forcing are independent and dating errors could lead to a wrong phasing of the two; modelling atmospheric CO_2 response to millennial scale forcing is a challenge (Schmittner et al., 2007; Menviel et al., 2008a) and it might not be simulated properly due to simplified model physics.

During the deglaciation, atmospheric CO_2 increases by respectively 44 ppmv, 50 ppmv and 26 ppmv in experiments $S1_{(Rem,P)}$, $S2_{(Rem,Br)}$ and $S3_{(Br,P)}$ (Table 2). There is a strong asymmetry in the pCO_2 response between the glaciation and the deglaciation. The brine parametrization forcing is asymmetric as the formation and sinking of very dense waters on the Antarctic shelf due to brine rejection is supposed to be minimal at the LGM due to the ice-sheet extent and during the deglaciation as the ice sheet melting adds freshwater to the coastal area. The oceanic P inventory also decreases during the deglaciation, but its pace is set on sea level change and it is thus a late player in the pCO_2 deglaciation change. In addition to the asymmetry in the forcing, the memory effects associated with the long response time scales of ocean–sediment interactions and the weathering–burial cycle (Goodwin and Ridgwell, 2010; Tschumi et al., 2011) prevents the CO_2 increase during the deglaciation.

In the following section, we further analyse the atmospheric CO_2 response using factorial experiments.

Table 2
Attribution of pCO_2 (ppmv), $\delta^{13}CO_2$ (permil) and $\delta^{13}C_{DIC}$ (permil) changes to processes for the period 125–20 ka B.P. and 20–0 ka B.P. $\delta^{13}C_{DIC}$ reflects the whole ocean change in $\delta^{13}C$ of DIC. As the experiments are performed with a sediment module, the processes described below include the pCO_2 response to sediment interactions. Physical processes denote all the processes included in experiment OC (T, S, ocean circulation and export production).

Processes	125–20 ka B.P.			20–0 ka B.P.		
	ΔCO_2	Δ ($\delta^{13}CO_2$)	Δ ($\delta^{13}C_{DIC}$)	ΔCO_2	Δ ($\delta^{13}CO_2$)	Δ ($\delta^{13}C_{DIC}$)
$S1_{(Rem,P)}$	−112	+0.078	−0.12	+44	−0.04	+0.12
$S2_{(Rem,Br)}$	−72	−0.39	−0.42	+50	+0.12	+0.16
$S3_{(Br,P)}$	−102	+0.033	−0.24	+26	+0.02	+0.18
Remineralization rate (REM–FE)	−31	−0.04	−0.02	+21	−0.054	−0.1
Brine param. (BR–FE)	−12	−0.1	−0.1	+2	0	−0.02
P inventory (PO–FE)	−50	+0.4	+0.2	+5	−0.2	−0.08
Terrestrial carbon (VG–FE)	+11	−0.1	−0.08	−17	+0.2	+0.18
Fe fertilization (FE–OC)	−10	+0.12	−0.002	+10	−0.14	−0.014
Physical processes (OC)	−31	−0.22	−0.24	+20	+0.18	+0.16
Shallow-water $CaCO_3$ deposition	–	–	–	+12	+0.026	+0.013

4.2. Factorial experiments

4.2.1. Physical forcings

As seen in Fig. 4a and Table 2, in response to physical forcings, atmospheric CO_2 decreases by 31 ppmv in experiment OC. The analysis of experiments TS and OC as well additional experiments performed with pre-industrial SST and without sediment module (cf Section 2.2) enables us to separate the different contributions to the atmospheric CO_2 decrease. In line with previous modelling studies, we obtain 27.5 ppmv CO_2 decrease due to the lower ocean temperature, compared to a reported range of 20–30 ppmv in the literature (Sigman and Boyle, 2000; Ridgwell, 2001; Köhler and Fischer, 2006; Brovkin et al., 2007). The 3% greater salinity at the LGM induces a CO_2 increase of 11 ppmv in close agreement with the literature range of 7–15 ppmv (Broecker and Peng, 1986; Sigman and Boyle, 2000; Ridgwell, 2001; Köhler and Fischer, 2006). Changes in sea ice extent do not have a significant impact on atmospheric CO_2 in our experiments, in agreement with results obtained with AOGCMs (Bopp et al., 2003; Chikamoto et al., 2012).

On the other hand, estimates of the CO_2 changes induced by ocean circulation vary greatly in the literature (+3 to −18 ppmv) (Ridgwell, 2001; Bopp et al., 2003; Brovkin et al., 2007; Tagliabue et al., 2009; Chikamoto et al., 2012). In general, ocean circulation changes in box models tend to lower CO_2 much more than in AOGCMs (Archer et al., 2003). Note that ocean–sediment interactions are not included in available AOGCM studies (Bopp et al., 2003; Tagliabue et al., 2009; Chikamoto et al., 2012). We attribute an LGM CO_2 decrease of 14 ppmv due to a weaker and shallower AMOC and a 6 ppmv CO_2 increase as a result of the globally lower export production (Table 2). Finally, an additional 6 ppmv CO_2 decrease is due to sediment interactions.

During the deglaciation (20–0 ka B.P.), atmospheric CO_2 increases by 20 ppmv in experiment OC (Fig. 4b, Table 2). This is considerably smaller than the simulated decrease of 31 ppmv during the much longer interval from 125 to 20 ka B.P. The difference is mainly due to ocean–sediment interactions, related imbalances in weathering and burial fluxes and the long time scales associated with these processes. Indeed, an experiment similar to OC performed without the sediment module leads to a 24 ppmv decrease until the LGM followed by an increase of equal magnitude.

4.2.2. Aeolian iron input

When aeolian iron input is transiently varied during the Last Glacial cycle, atmospheric CO_2 varies by about 10 ppmv (experiment FE, Fig. 4c, Table 2). Ocean–sediment interactions contribute about 40% to these changes. Following the iron record from EPICA Dome C ice core (Wolff et al., 2006) (Fig. 1), the iron impact on atmospheric CO_2 is significant between 70 and 16 ka B.P.

As iron is a limiting nutrient in the High Nutrient Low Chlorophyll regions (Southern Ocean, Eastern Equatorial Pacific and North Pacific), a greater input of iron leads to an increase in export production in these regions (Fig. 5i) and therefore to a lower pCO_2. Changes in export production following iron input are discussed in Section 5.2.

The relative magnitude of the CO_2 decrease as well as the spatial distribution of the export production changes due to the iron input obtained in this study are in general agreement with the results obtained with the state-of-the-art ocean biogeochemistry model PISCES (Bopp et al., 2003; Tagliabue et al., 2009) despite the lack of a sediment module in their study. A doubling of the iron deposition in the Southern Ocean (FEx2) or an increase in the iron flux to the South Pacific Ocean (FEsP) would further lower atmospheric CO_2 by 2 ppmv compared to experiment FE. Some slight changes in the iron forcing would thus not modify significantly the results presented above. On the other hand, the impact on atmospheric CO_2

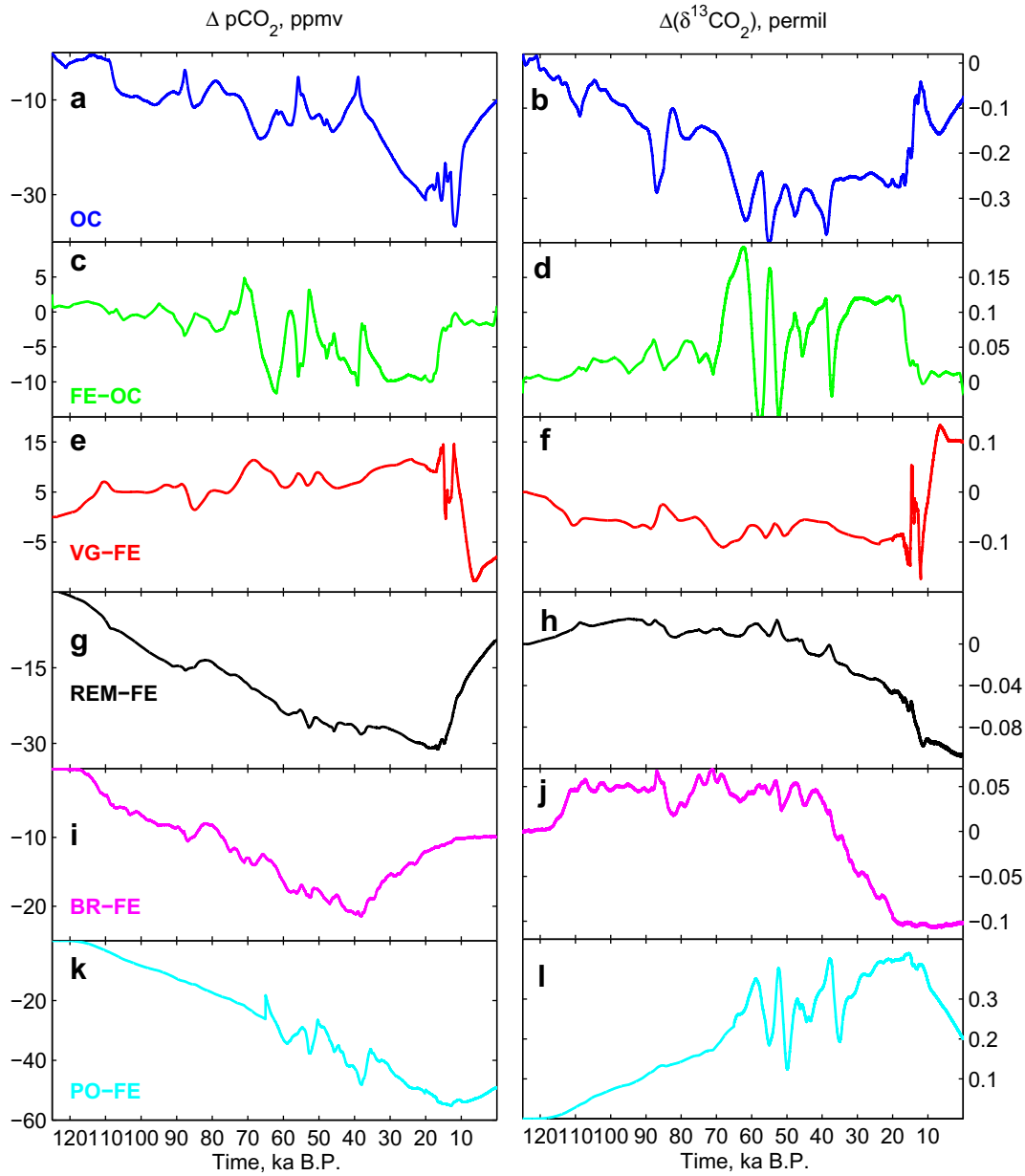

Fig. 4. Time series of (left) atmospheric CO_2 anomalies (ppmv) and (right) atmospheric $\delta^{13}CO_2$ anomalies (permil) for experiments (a,b) OC, (c,d) FE−OC, (e,f) VG−FE, (g,h) REM−FE, (i,j) BR−FE and (k,l) PO−FE.

and export production of uncertainties in model parameters, such as iron ligand concentration, are discussed by Parekh et al. (2008) and appear more substantial (5–10 ppmv).

4.2.3. Land carbon reservoir changes

In experiment VG, we apply an idealised 340 GtC release from the terrestrial reservoir, scaled on global temperature change, from the Last Interglacial to the LGM and a corresponding uptake during the deglaciation (Fig. 1). As a result, atmospheric CO_2 is 11 ppmv higher in experiment VG than in experiment FE at the LGM (Fig. 4e). Without sediment interactions, the release of 340 GtC leads to an atmospheric CO_2 increase of 24 ppmv. In other words, $CaCO_3$ compensation mitigates about half of the atmospheric CO_2 increase due to terrestrial carbon release. The land carbon uptake during the deglaciation causes a 17 ppmv decrease. Thus, a smaller fraction of the CO_2 perturbation is mitigated by $CaCO_3$ compensation during the deglacial period compared to the much longer glaciation.

4.2.4. Changes in the remineralization depth

When the depth above which 63% of the Particulate Organic Matter (POM) is remineralized increases and a slower rate of Dissolved Organic Matter (DOM) remineralization is imposed (experiment REM) (Fig. 4g), atmospheric CO_2 decreases by an additional 31 ppmv compared to experiment FE. The greater depth of the POM remineralization induces a 27 ppmv decrease while the slower rate of DOM contributes only 4 ppmv. The overall decrease and the small role of DOM is in agreement with Matsumoto (2007), who obtained a 35 ppmv CO_2 decrease following the implementation of temperature-dependent POM and DOM remineralization for glacial conditions. As the changes in remineralization rates are scaled on

the simulated ocean temperature, the CO_2 decrease occurs gradually over the 105,000 years of the glaciation.

The lower CO_2 is due to lower DIC and higher ALK concentrations in the surface ocean in REM than in FE at the LGM. As the remineralization occurs deeper at the LGM in experiment REM compared to experiment FE, the DIC upwelled to the surface is reduced. The upwelling of DIC is particularly weaker in the Eastern Equatorial Pacific (EEP), the Eastern Equatorial Atlantic (EEA), the Southern Ocean and the North Pacific. As a result of the reduced upwelled DIC and greater surface alkalinity, the CO_2 flux out of the ocean is reduced by 100% in the Southern Ocean, by 50% in the EEP and by 17% in the EEA. In addition the CO_2 flux into the North Pacific and the North Atlantic is strengthened by respectively 40% and 10%.

The combined effect of changing POM and DOM remineralization rates during the deglaciation leads to a CO_2 increase of 21 ppmv (Fig. 4g), thus 32% smaller than the decrease until the LGM. This difference in amplitude is primarily due to the long, multi-millennial response scale to perturbations in ocean sediment and burial processes as well as the different duration of the glacial and deglacial period.

4.2.5. Brine rejection parametrization

The transport of brines to the deep parts of the Atlantic and Pacific Southern Ocean leads to a 0.3 increase in salinity in the deep ocean, while the surface salinity decreases by about 0.15. This surface salinity change is too small to have a significant impact on pCO_2, but induces a slight weakening of AABW formation.

As DIC-rich water is directly transported to depth in the Southern Ocean by the brine mechanism, a greater surface to deep DIC gradient in both the Atlantic and Pacific Ocean is obtained in experiment BR compared to FE. At 40 ka B.P., there is a positive DIC anomaly at depth in the Atlantic (+12 μmol/L) and Pacific (+41 μmol/L) oceans, while there is a negative DIC anomaly at the surface (−55 μmol/L) of both oceans compared to simulation FE without the brine parametrization.

The greater DIC than alkalinity decrease at the ocean's surface in experiment BR compared to experiment FE leads to a 10 to 20 ppmv lower atmospheric CO_2 (Fig. 4i). The maximum pCO_2 decrease (−23 ppmv) is obtained at about 40 ka B.P., after which pCO_2 increases to reach an anomaly of −12 ppmv at the LGM. During the deglaciation pCO_2 only increases by 2 ppmv. At the end of experiment BR (0 ka B.P.), the deep DIC content in both the Pacific and Atlantic oceans is still greater than at the beginning of the experiment (125 ka B.P.). A stronger ventilation of both the Atlantic and Pacific oceans during the deglaciation could potentially lead to a pCO_2 increase of the remaining balance of 10 ppmv.

The pCO_2 evolution in experiment BR reflects the changes in the forcing parameter *frac* (Fig. 1), which is based on the evolution of the Antarctic ice sheet and the global sea level during the glaciation. Uncertainties in the timing and amplitude of the brine rejection parametrization are further discussed in Section 7.

4.2.6. Oceanic phosphate inventory

When the global oceanic phosphate inventory increases by 10% (Fig. 1d), atmospheric CO_2 decreases by an additional 50 ppmv (experiment PO compared to FE) (Fig. 4k). The pCO_2 decrease is gradual from 112 to 20 ka B.P. Tschumi et al. (2011) already presented the results of a step-like 30% increase in oceanic phosphate inventory and showed that about 60% of the atmospheric CO_2 decrease was due to ocean–sediment interactions.

By increasing the oceanic phosphate inventory gradually by 10% we obtain the same result as the one obtained when increasing the reservoir abruptly by 30% as done in Tschumi et al. (2011). As the oceanic phosphate content increases, export production increases, which lowers atmospheric CO_2. However export production is also limited by other factors such as light, Fe or Si thus restricting the impact of changes in phosphate content on atmospheric CO_2.

During the deglaciation, atmospheric CO_2 increases by only 5 ppmv. As the residence time of phosphorus in the ocean is in the order of 20 ka (Colman and Holland, 2000), export production is still higher during the termination in experiment PO than in experiment FE. Only at 6 ka B.P. do they become equivalent. The nutrient utilisation reaches its maximum at 10 ka B.P. In addition, the higher export of organic matter and $CaCO_3$ during the glaciation leads to a significant increase in organic carbon and $CaCO_3$ burial, thus effectively lowering the carbon content of the ocean.

In summary, the increase in phosphate inventory contributes about 50 ppmv while the changes in physical forcings and in the remineralization depth contribute about 30 ppmv each to the simulated CO_2 decrease from 125 to 20 ka B.P. The corresponding contributions by iron fertilization and brine rejection are not negligible but with a magnitude of around 10 ppmv smaller. A contrasting picture emerges for the deglacial rise. The contribution by changes in the phosphate inventory is very small due to the long time scales of the weathering–burial cycle. The largest positive contributions for the deglaciation are from changes in physical forcings and remineralization depth. It is evident that the system is not at equilibrium at 0 ka B.P. and that the degree of equilibration differs among different mechanisms.

5. Export production and deep $[CO_3^{2-}]$ changes at the Last Glacial Maximum

5.1. Experiments with all the forcings and comparison with paleo-proxies

5.1.1. Export production

At the LGM, the globally averaged export production is respectively 7% and 14% lower in experiments $S1_{(Rem,P)}$ and $S2_{(Rem,Br)}$ compared to pre-industrial times, while export production is 6% greater in experiment $S3_{(Br,P)}$. In experiments S1–3, export production decreases at high Northern and Southern latitudes: in the North Atlantic (−100%), the North Pacific (−6:−24%) and the Southern Ocean (47°S–70°S) (−27:−33%), in agreement with paleo-proxies (Kohfeld et al., 2005) (Fig. 5). The 3 experiments also display a greater export production in the Eastern Equatorial Pacific (EEP) and a slight decrease in the tropical Atlantic north of the equator. Paleo-proxies do not display a consistent picture in the EEP, however they suggest greater export off the North African coast contrarily to our model results.

In the Southern Ocean north of the polar front (40°S–45°S), export production is greater at the LGM in experiments $S1_{(Rem,P)}$ (+5%) and $S3_{(Br,P)}$ (+19%) in agreement with paleo-proxies (Kohfeld et al., 2005), whereas it is weaker in experiment $S2_{(Rem,Br)}$ (−5%). In addition, only experiment $S3_{(Br,P)}$ simulates greater export at the LGM in the south equatorial Atlantic.

A globally greater export production at the LGM seems to be in better agreement with paleo-proxies as obtained in $S3_{(Br,P)}$. This is achieved by increasing the oceanic P inventory and increasing the aeolian iron input. On the other hand, increasing the remineralization depth and to a lesser extent stratifying the ocean, as it is done with the brine parametrization, induce a weaker export production.

5.1.2. Deep-ocean carbonate ion concentration

Experiment $S1_{(Rem,P)}$ simulates the greatest deep $[CO_3^{2-}]$ increase at the LGM (Fig. 6), while experiment $S3_{(Br,P)}$ displays the weakest. The three experiments show a negative deep $[CO_3^{2-}]$ anomaly in the North Atlantic and experiments $S1_{(Rem,P)}$ and $S2_{(Rem,Br)}$ display

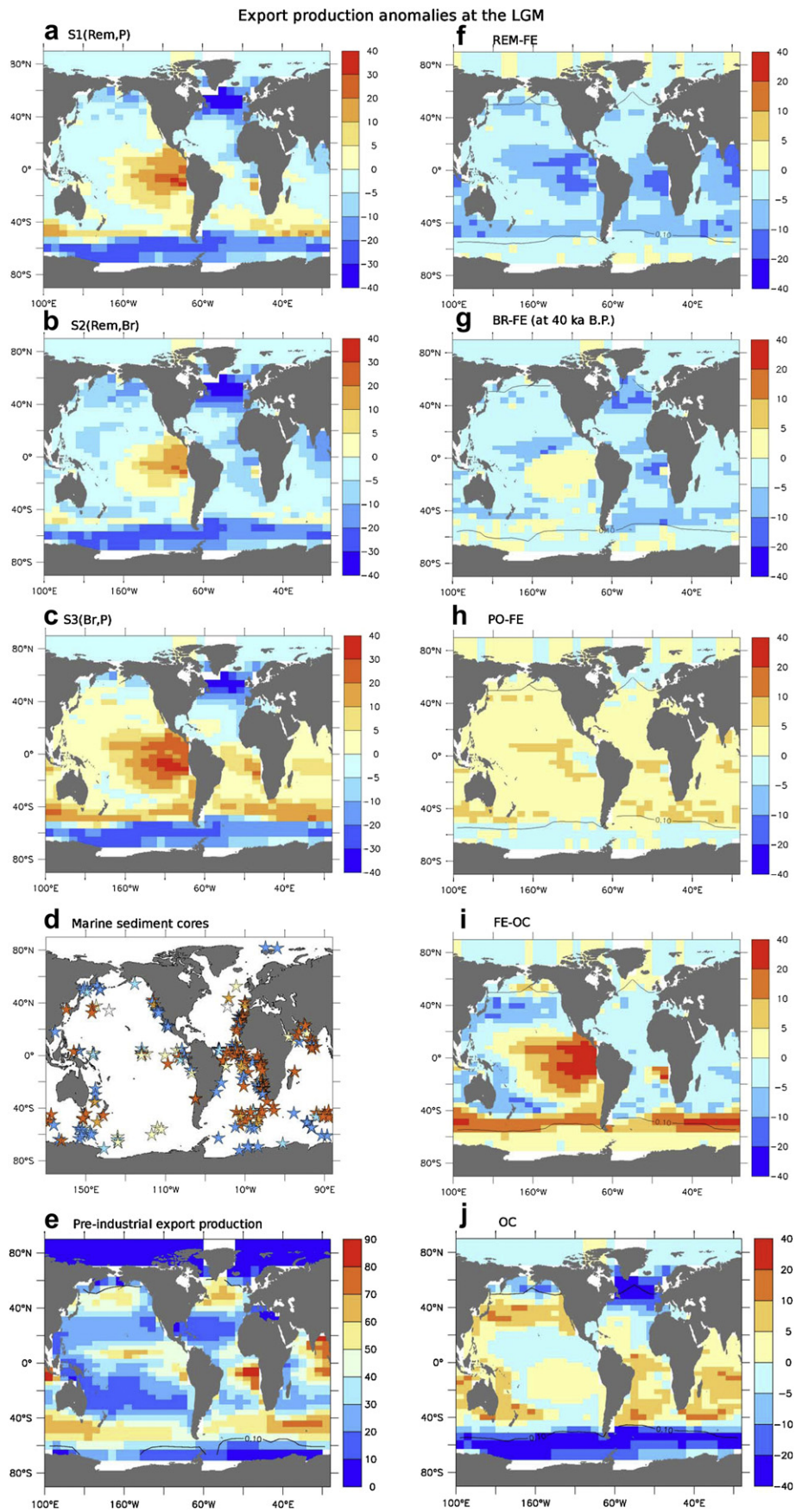
Export production anomalies at the LGM
a S1(Rem,P)
b S2(Rem,Br)
c S3(Br,P)
d Marine sediment cores
e Pre-industrial export production
f REM-FE
g BR-FE (at 40 ka B.P.)
h PO-FE
i FE-OC
j OC
80°N
40°N
0°
40°S
80°S
100°E
160°W
60°W
40°E
150°E
110°W
10°W
90°E

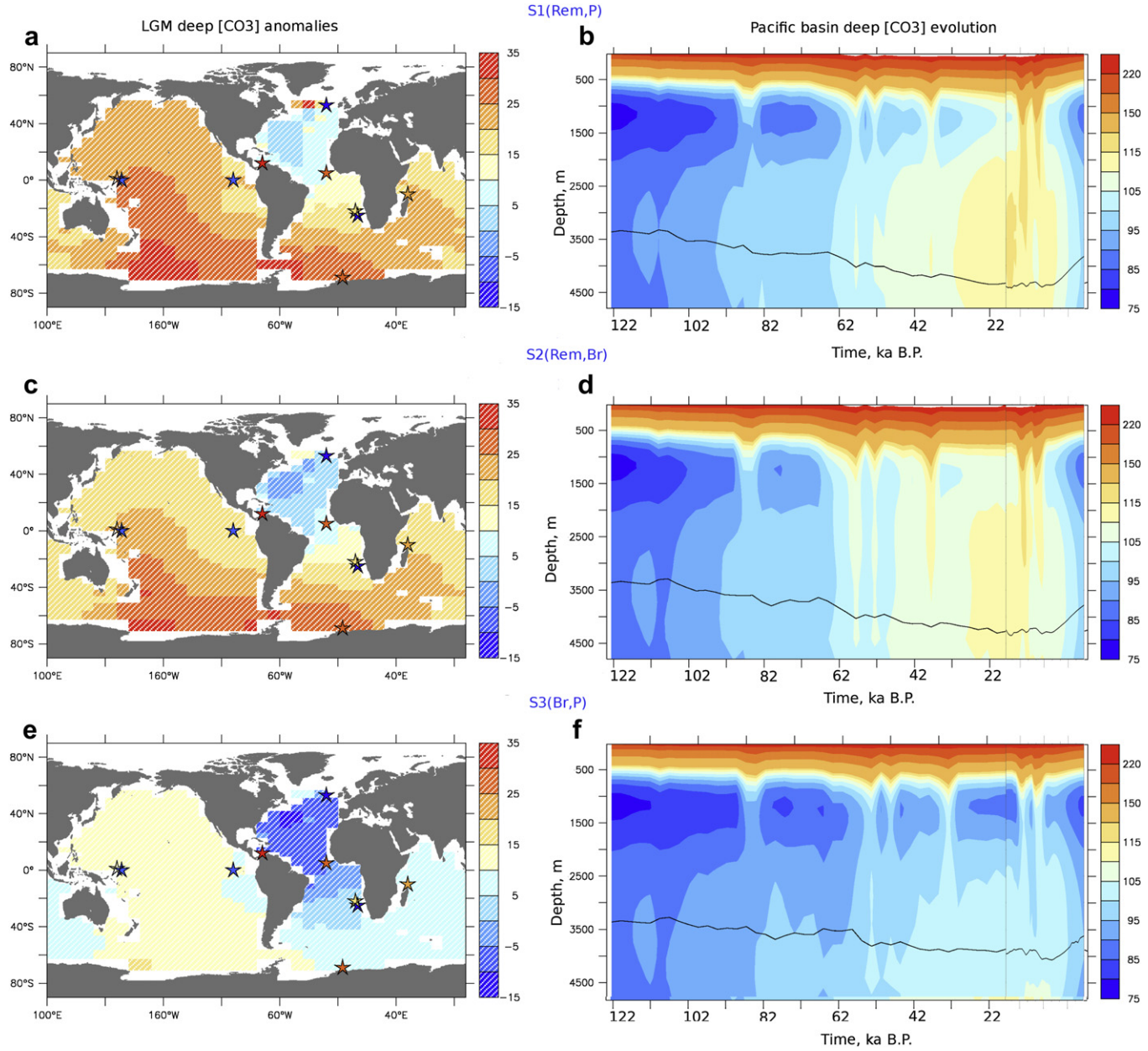

Fig. 6. (left) Deep (2500–5000 m) $[CO_3^{2-}]$ anomalies (μmol/L) at the LGM compared to pre-industrial times (20–0 ka B.P.) for experiments (a) $S1_{(Rem,P)}$, (c) $S2_{(Rem,Br)}$ and (e) $S3_{(Br,P)}$. Overlaid are $[CO_3^{2-}]$ LGM anomaly estimates from marine sediment cores (from West to East) MW91-9 GGC48 (Yu et al., 2010), V28-238 (Sanyal et al., 1995), RC13-214 (Marchitto et al., 2005), VM28-122 and BOFS 8K (Yu et al., 2010), ODP 668B, GeoB 1220, GeoB 1214 and GeoB 1034 (Hönisch et al., 2008), PS 1506 (Rickaby et al., 2010) and WIND28K (Yu et al., 2010). (right) Hovmöller diagrams (depth, m vs time, ka B.P.) as obtained in experiments (b) $S1_{(Rem,P)}$, (d) $S2_{(Rem,Br)}$ and (f) $S3_{(Br,P)}$ for $[CO_3^{2-}]$ (μmol/kg) averaged over the Pacific basin. The black line represents the depth of the calcite saturation horizon.

a significant (∼+30 μmol/L) positive anomaly in the Southern Ocean. Experiment $S2_{(Rem,Br)}$ has the most similarities with paleo-proxies (Sanyal et al., 1995; Marchitto et al., 2005; Hönisch et al., 2008; Rickaby et al., 2010; Yu et al., 2010), but the scarcity of the proxies and their high variability around the LGM prevent any firm conclusion.

The time evolution of the $[CO_3^{2-}]$ changes in the Pacific basin is shown in Fig. 6 right as well as the calcite saturation horizon for experiments $S1_{(Rem,P)}$ (b), $S2_{(Rem,Br)}$ (d) and $S3_{(Br,P)}$ (f). Below 2000 m, $[CO_3^{2-}]$ gradually increases over the glaciation until reaching an anomaly of about +21 μmol/L at the LGM in

Fig. 5. (left) Export production anomalies (gC/m^2/yr) between the LGM and the pre-industrial state for experiments (a) $S1_{(Rem,P)}$, (b) $S2_{(Rem,Br)}$, (c) $S3_{(Br,P)}$ and (d) as suggested by paleo-proxies (Kohfeld et al., 2005). Orange and yellow respectively indicate cores with higher and slightly higher LGM export compared to the late Holocene. White indicates no significant changes. Dark blue and light blue respectively represent cores with lower and slightly lower LGM export. (e) Marine export production (gC/m^2/yr) as simulated during pre-industrial times. (right) Export production anomalies at the LGM for experiments (f) REM–FE, (g) BR–FE, (h) PO–FE and (i) FE–OC. (j) Export production anomalies (gC/m^2/yr) between experiment OC at the LGM and the pre-industrial state. For experiments BR–FE (f), anomalies at 40 ka B.P. are shown as *frac* is maximal at that time. The 0.1 m annual sea ice contour is also shown in graphs e–j. (For interpretation of the references to colour in this figure legend, the reader is referred to the web version of this article.)

experiments $S1_{(Rem,P)}$ and $S2_{(Rem,Br)}$. In experiment $S3_{(Br,P)}$, the $[CO_3^{2-}]$ anomaly under 2000 m is of +10 μmol/L. Due to the deep $[CO_3^{2-}]$ increase, the calcite saturation horizon in the Pacific basin deepens respectively by 800 m, 650 m and 400 m in experiments $S1_{(Rem,P)}$, $S2_{(Rem,Br)}$ and $S3_{(Br,P)}$ during the glaciation. During the deglaciation the deep $[CO_3^{2-}]$ decreases in all simulations S1–3, however it does not reach its initial value. For the three simulations about 50% of the deep $[CO_3^{2-}]$ anomaly is still present at the end of the deglaciation. In our experiments, at 0 ka B.P., the ocean–sediment system is thus not in equilibrium and it is still recovering from the deglaciation changes. This delayed response affects not only carbonate ion concentration but also atmospheric CO_2 as discussed in the previous section.

Below we describe in further details factorial experiments with respect to nutrients distribution, export production and deep $[CO_3^{2-}]$ variations.

5.2. Factorial experiments

5.2.1. Changes in remineralization depth

A deepening of the remineralization profile of POM leads to a lowering of DIC and phosphate content in the upper 1000 m in the Pacific and upper 3000 m in the Atlantic, while increasing their content at depths. In an idealised experiment without any changes in ocean circulation, a greater remineralization depth induces a phosphate concentration increase in the deep North Pacific (~+0.20 μmol/L), while leading to a decrease in the deep North

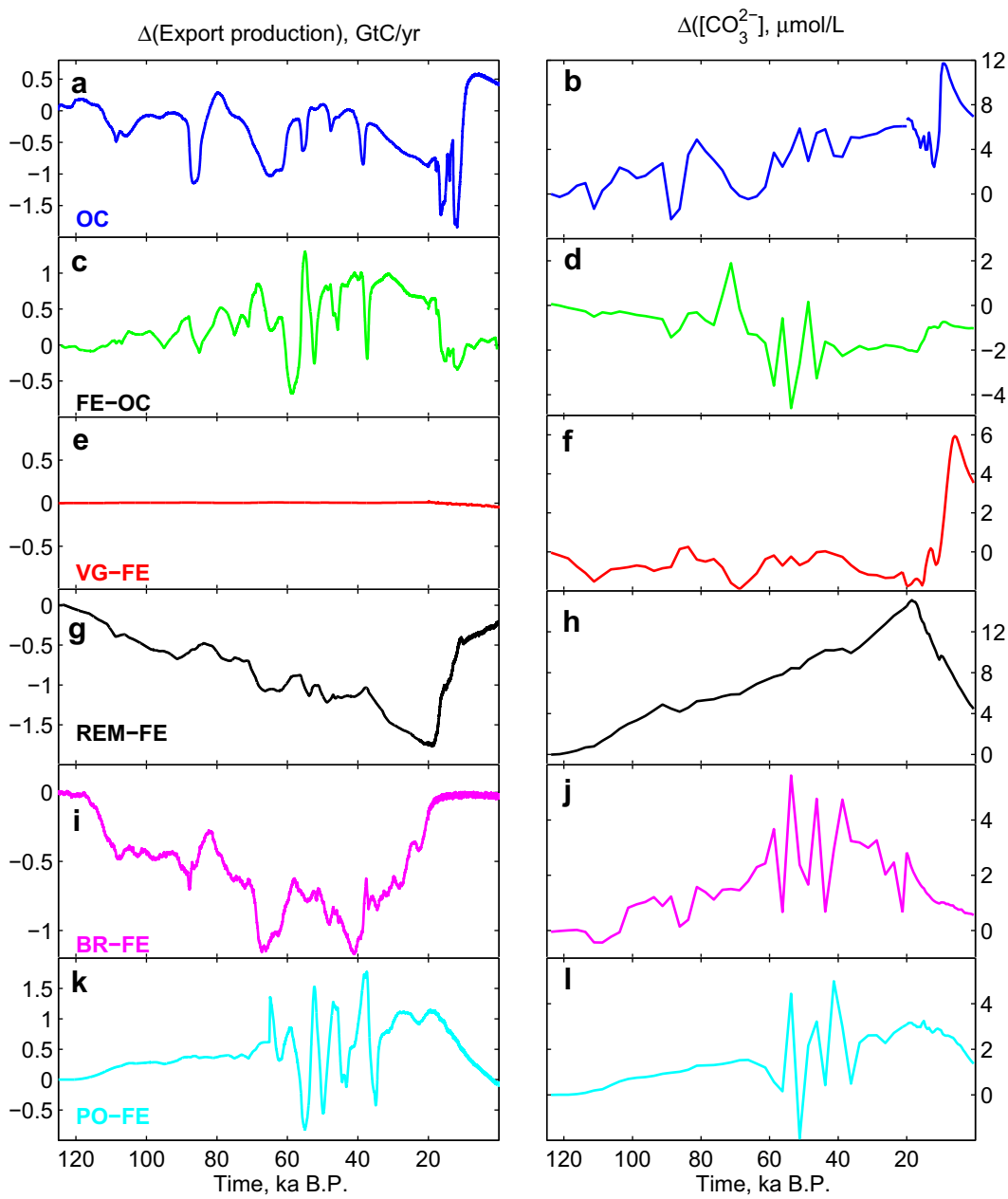

Fig. 7. Time series of (left) export production anomalies (GtC/yr) and (right) globally averaged deep (≥3000 m) $[CO_3^{2-}]$ anomalies (μmol/L) for experiments (a,b) OC, (c,d) FE–OC, (e,f) VG–FE, (g,h) REM–FE, (i,j) BR–FE and (k,l) PO–FE.

Atlantic (∼−0.20 μmol/L), in agreement with the results of Matsumoto (2007). As the AMOC is weaker and shallower at the LGM in our experiments, the deep phosphate concentration actually decreases in the Southern Ocean, while increasing in the North Atlantic.

The reduced nutrient supply to the surface induces an additional 15% decrease in the global export of organic matter and $CaCO_3$ at the LGM in REM compared to FE (Fig. 7g). On the other hand, the opal production remains the same. As seen in Fig. 5f, the export production is particularly lowered in the upwelling regions of the Eastern Equatorial Pacific and Atlantic as well as north of the polar front in the Southern Ocean. In contrast, the proxy records suggest an increase in export in these regions. Thus other factors than a deepening of the remineralization depth were most likely responsible for the reconstructed higher export rates at the LGM.

The reduced $CaCO_3$ precipitation causes an alkalinity increase at the ocean's surface, a temporary reduction in $CaCO_3$ burial that leads to a whole ocean alkalinity increase and to a deepening of the calcite saturation horizon (Broecker and Peng, 1987; Tschumi et al., 2011). As a result, deep $[CO_3^{2-}]$ is 14 μmol/L higher in REM than in FE at 20 ka B.P. (Fig. 7h). The difference is most pronounced in the Southern Ocean (+20 μmol/L) and weakest in the North Pacific (+10 μmol/L). Preservation of $CaCO_3$ in the sediments is enhanced in REM compared to FE and the sediment $CaCO_3$ stock is about 110 GtC larger at the LGM.

5.2.2. Brine parametrization

The implementation of the brine parametrization leads to a direct transport of nutrients from the surface to the deep ocean in the Southern Ocean. As the imposed *frac* is maximal at 40 ka B.P. and minimal at 20 ka B.P., the maximum export production anomaly is obtained at 40 ka B.P. in experiment BR (Fig. 7i). The greater nutrient content in the deep ocean and lower content at the surface induce an 8% global export production decrease at 40 ka B.P. in experiment BR compared to experiment FE (Fig. 5g). Export production decreases particularly in the Atlantic side of the Southern Ocean and the Eastern Equatorial Atlantic. As with the remineralization mechanism, the brine mechanism as included in our model yields a pattern in export that is in contrast to the proxy-based pattern. Taken at face value, this may suggest that the brine mechanism did not play a dominant role in regulating the evolution of export productivity and atmospheric CO_2 since the LGM.

As the silicate content also increases at depth while decreasing at the surface, the opal production is 10.2% lower at the LGM in BR than in FE. Relatively the $CaCO_3$ export decreases less (−7.8%) leading to a relative lower decrease in alkalinity (−37 μmol/L) than in DIC (−55 μmol/L) at the surface ocean, which promotes the simulated pCO_2 decrease.

The alkalinity content increases in the deep ocean (+29 μmol/L), relatively more than DIC (+23 μmol/L), which leads to a slightly greater deep $[CO_3^{2-}]$ content (+3 μmol/L) in BR compared to FE at 40 ka B.P. (Fig. 7j). Preservation of $CaCO_3$ in the sediments is thus enhanced and the sediment $CaCO_3$ stock is about 70 GtC larger at the LGM in experiment BR than in experiment FE.

5.2.3. Increase in oceanic phosphate inventory

A greater oceanic phosphate inventory drives a 10% global increase in export production in experiment PO compared to experiment FE at the LGM in agreement with previous studies (Tschumi et al., 2011) (Fig. 7k). The $CaCO_3$ export similarly increases by 8%, while the opal production is 3% greater. Tschumi et al. (2011) find that the oceanic phosphate inventory and export production relaxes back with a time scale of about 15 ka to its initial state after a pulse-like input of phosphate. As our change in oceanic phosphate inventory is progressive over about 100 ka, the export production also slowly increases over that time period, even with the sediment model. At the LGM, the export production increases slightly everywhere in the latitudinal band 40°S–40°N (Fig. 5h) compared to experiment FE, except south of the annual sea ice edge in the Southern Ocean where export production is limited by light. An enhancement of export production at mid and low latitudes as simulated by an increase in P inventory goes in the same direction as suggested by the proxies.

As the organic matter and $CaCO_3$ production are greater, the organic carbon and $CaCO_3$ burials increase. A slight increase (+3 μmol/L) in deep $[CO_3^{2-}]$ content is observed at the LGM in experiment PO compared to experiment FE (Fig. 7l) and the sediment $CaCO_3$ stock is about 90 GtC larger.

5.2.4. Iron fertilization

The greater input of iron into the ocean during the glaciation leads to an increase in marine export production. The export production anomaly in between experiment FE and experiment OC is the greatest at ∼40 ka B.P. and 30 ka B.P. (Fig. 7c), which corresponds to times of high dust input and relatively warm conditions at high southern latitudes compared with the LGM. The reduced sea ice extent in the Southern Ocean at these times compared to the LGM is instrumental in leading to higher export production. At 30 ka B.P. export production is about 20% higher than during pre-industrial times in the Southern Ocean north of the annual sea ice edge (40°S–50°S). The input of iron has the greatest impact on export production in the HNLC region. At the LGM export production is thus higher in experiment FE compared to experiment OC in the Southern Ocean (+33%), particularly north of the polar front and the Eastern Equatorial Pacific (+46%) (Fig. 5i). Our results suggest that iron fertilization contributed to the reconstructed high LGM export north of the Southern Ocean polar front and in parts of the Pacific, while it generally left a small imprint south of the polar front and in the Atlantic. However, in experiment FE global export production is still globally 3% reduced at the LGM compared to pre-industrial times. On the other hand, following the iron input, opal production increases only in the latitudinal band 45°S–70°S by +12%. Everywhere else opal production is limited by silicic acid availability.

The input of aeolian iron into the ocean leads to a 2 μmol/L decrease of deep $[CO_3^{2-}]$ at the LGM (Fig. 7d).

5.2.5. Changes in terrestrial carbon reservoir

Changes in terrestrial carbon reservoir do not have any impact on export production (Fig. 7e), however they induce a small (−2 μmol/L) decrease in deep $[CO_3^{2-}]$ during the glaciation. During the deglaciation, land carbon uptake decreases pCO_2 and leads to a relative increase in ALK at depth with respect to DIC. Following the $CaCO_3$ compensation mechanism, a strong (+8 μmol/L) increase in deep $[CO_3^{2-}]$ is thus simulated during the termination (Fig. 7f).

5.2.6. Physical forcings

The decrease in ocean temperature, sea-ice advance at the poles and weaker AMOC leads to reduced (−7%) export production at the LGM in experiment OC compared to pre-industrial times (Fig. 7a). Due to sea ice advance, export production is halved in the Southern Ocean and the North Atlantic (Fig. 5j). On the other hand, due to the greater meridional advection of nutrients in the euphotic zone, export production is 9% greater at low latitudes at the LGM. In experiment OC deep $[CO_3^{2-}]$ increases by about 6 μmol/L during the glaciation (Fig. 7b).

In conclusion, the different forcings leave distinct spatial and temporal patterns in export production and the distribution of

carbonate ion. Clearly, spatially resolved proxy-reconstructions provide additional constraints to evaluate the plausibility of model results and of hypothetically applied forcings and mechanisms.

6. $\delta^{13}CO_2$ and $\delta^{13}C_{DIC}$

6.1. Experiments with all the forcings and comparison with paleo-proxies

6.1.1. $\delta^{13}CO_2$

As seen in Fig. 3, atmospheric $\delta^{13}CO_2$ increases over the glaciation in experiments $S1_{(Rem,P)}$ (+0.078 permil) and $S3_{(Br,P)}$ (+0.033 permil) while decreasing in experiment $S2_{(Rem,Br)}$ (−0.39 permil). Analyses of air bubbles trapped in Antarctic ice cores indicate that atmospheric $\delta^{13}CO_2$ increased by ~0.2 permil over the glaciation (Schneider, 2011). Experiments $S1_{(Rem,P)}$ and $S3_{(Br,P)}$ would thus be in better agreement with paleo-proxies than experiment $S2_{(Rem,Br)}$ over the glaciation.

These $\delta^{13}CO_2$ variations are the results of competing effects: iron fertilization and the greater phosphate inventory both lead to positive $\delta^{13}CO_2$ anomalies, while the reduced terrestrial carbon storage during glacial times, the weaker ocean circulation, the greater remineralization depth and the brine parametrization induce a negative $\delta^{13}CO_2$ anomaly.

The $\delta^{13}CO_2$ variations simulated during the deglaciation are in relative agreement with the paleo-proxy record from EPICA Dome C ice core (Elsig et al., 2009; Lourantou et al., 2010; Schmitt et al., 2012) for all experiments S1–3. The model simulations and the paleo-proxies show a $\delta^{13}CO_2$ negative anomaly for H1 and YD. However, our three simulations display a significant positive $\delta^{13}CO_2$ anomaly during the Bölling–Allerod, which is seen in the Lourantou et al. (2010) record but not in the averaged data from Schmitt et al. (2012). This strong positive anomaly is due to both the global SST increase and the resumption of the AMOC after H1.

6.1.2. $\delta^{13}C_{DIC}$

As seen in Fig. 8 left, modelled $\delta^{13}C_{DIC}$ in the deep Atlantic basin (≥3000 m) decreases by respectively 0.5, 0.8 and 0.6 permil for experiments $S1_{(Rem,P)}$, $S2_{(Rem,Br)}$ and $S3_{(Br,P)}$ over the glaciation, while the paleo-proxies suggest a 0.4 to 0.6 permil drop (Lisiecki et al., 2008; Oliver et al., 2010). Simulations S1–3 are able to represent some of the strong negative $\delta^{13}C_{DIC}$ excursions centred at about 110, 90 and 65 ka B.P., reinforcing the idea that part of these strong negative excursions are due to significant changes in the strength of the AMOC. The negative excursions are the greatest in experiment $S2_{(Rem,Br)}$ and the smallest in experiment $S1_{(Rem,P)}$. None of the three simulations is able to represent the reconstructed abrupt increase in $\delta^{13}C_{DIC}$ in the deep Atlantic around 60 ka B.P. This

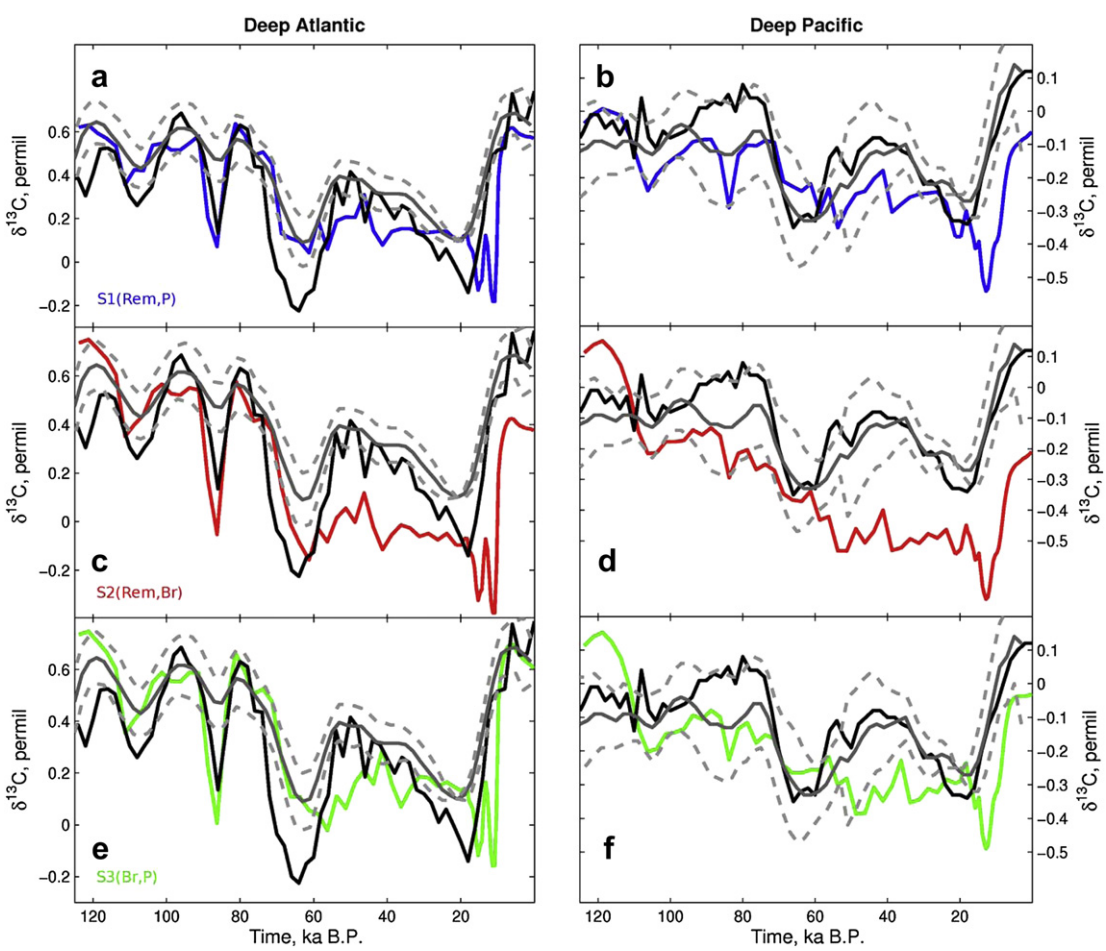

Fig. 8. Time series of $\delta^{13}C_{DIC}$ for $S1_{(Rem,P)}$ (a,b), $S2_{(Rem,Br)}$ (c,d) and $S3_{(Br,P)}$ (e,f) compared to benthic $\delta^{13}C$ record compiled by Lisiecki et al. (2008) (black) and Oliver et al. (2010) (grey) in (left) the deep Atlantic (2500–5000 m) and (right) the deep Pacific (2500–5000 m). The solid grey line represents the mean $\delta^{13}C_{DIC}$ and the dashed line the 2X standard error (Oliver et al., 2010).

may indicate that circulation and water masses changes are not represented correctly by the model for this period.

During the deglaciation, the simulated deep $\delta^{13}C_{DIC}$ in the Atlantic increases by 0.5 permil for experiments S1–3, while the paleo-proxies suggest a 0.5 to 0.8 permil increase (Lisiecki et al., 2008; Oliver et al., 2010). In addition, the simulated deep $\delta^{13}C_{DIC}$ displays negative anomalies associated with the AMOC weakening of H1 and the YD. A strong negative dip is seen in the Lisiecki et al. (2008) record that could be associated with H1. These negative excursions are also seen in some high resolution marine sediment cores of the North Atlantic (e.g. (Skinner and Shackleton, 2004; Martrat et al., 2007)).

In the deep Pacific basin, the modelled $\delta^{13}C_{DIC}$ decreases by 0.4, 0.6 and 0.4 permil until 20 ka B.P. in respectively experiments $S1_{(Rem,P)}$, $S2_{(Rem,Br)}$ and $S3_{(Br,P)}$ (Fig. 8 right), while the paleo-proxies show a ~0.3 permil decrease (Lisiecki et al., 2008; Oliver et al., 2010). In addition, there are significant differences between the shape of the simulated $\delta^{13}C_{DIC}$ and the proxy data. Notably, simulations S1–3 show a significant $\delta^{13}C_{DIC}$ decrease at 110 ka B.P., that is not seen in the paleo-proxy data. This $\delta^{13}C_{DIC}$ decrease at 110 ka is enhanced in the simulations forced by the brine rejection mechanism ($S2_{(Rem,Br)}$ and $S3_{(Br,P)}$). Apparently, the prescribed early onset of the brine mechanism is not consistent with the deep Pacific $\delta^{13}C_{DIC}$ record.

The $\delta^{13}C_{DIC}$ simulated in experiment $S1_{(Rem,P)}$ bears the most resemblance with the proxy record while the one simulated in experiment $S2_{(Rem,Br)}$ shows the least agreement. For the three experiments, the simulated $\delta^{13}C_{DIC}$ decreases even further during the first stage of the deglaciation in contradiction with the paleo-proxy. The total $\delta^{13}C_{DIC}$ increase during the deglaciation amounts to about 0.3 permil compared to 0.4 permil for the paleo-proxy (Lisiecki et al., 2008; Oliver et al., 2010).

Increasing the carbon uptake during the deglaciation from 340 to 660 GtC would further increase $\delta^{13}C_{DIC}$ in both the deep Atlantic and deep Pacific by 0.1 permil (not shown), however it would not significantly impact the $\delta^{13}C_{DIC}$ evolution during the glaciation. Indeed, the isotopic perturbation is largely removed from the atmosphere–land–ocean system through sedimentary burial. Of course, a greater release of carbon from the terrestrial biosphere has an impact on atmospheric CO_2 as well. If the terrestrial carbon release during the glaciation is equivalent to 660 GtC, then CO_2 is about 6 ppmv higher at the LGM.

Next, the spatial pattern of the $\delta^{13}C_{DIC}$ anomalies is discussed. Fig. 9 shows maps of $\delta^{13}C_{DIC}$ anomaly between the LGM and pre-industrial times in the deep (2500–5000 m) ocean as well as averaged over the Atlantic basin. Aside from a few marine sediment cores, model and paleo-proxy data tend to agree on a strong (≥0.7 permil) $\delta^{13}C_{DIC}$ negative anomaly at the LGM in the deep North Atlantic Ocean, which progressively gets smaller when moving towards the south Atlantic. However, in the deep South Atlantic Ocean, poleward of 40°S, experiments S1–3 simulate a $\delta^{13}C_{DIC}$ anomaly of −0.2 to −0.4 permil at the LGM, whereas benthic $\delta^{13}C$ data suggest an anomaly of about −0.9 permil (Charles et al., 1991, 1996; Ninnemann and Charles, 2002; Hodell et al., 2003). Neither the simulations with brine parametrization ($S2_{(Rem,Br)}$ and $S3_{(Br,P)}$) nor the ones with greater oceanic phosphate inventory ($S1_{(Rem,P)}$ and $S3_{(Br,P)}$) simulate such a strong negative $\delta^{13}C_{DIC}$ anomaly. It is experiment $S2_{(Rem,Br)}$, forced with a slower remineralization rate and the brine parametrization, which displays the stronger negative $\delta^{13}C_{DIC}$ anomaly despite simulating the lowest export production in the Southern Ocean (Fig. 5b). A greater $\delta^{13}C_{DIC}$ anomaly in the deep South Atlantic could potentially be obtained in experiment $S3_{(Br,P)}$ with a different timing of the brine parametrization.

Below we discuss in greater details the impact on $\delta^{13}CO_2$ and $\delta^{13}C_{DIC}$ of the main forcings.

6.2. Factorial experiments

6.2.1. Changes in the remineralization depth

The deeper remineralization of POM in REM during the glaciation and the consequent greater transport of light carbon to the deep ocean induces a vertical redistribution of ^{13}C. At the LGM, a positive $\delta^{13}C_{DIC}$ anomaly (~+0.15 permil) is generated at intermediate depth in the equatorial ocean, where the bulk of the remineralization generally occurs, while a negative $\delta^{13}C_{DIC}$ anomaly is simulated at depth in both the Atlantic and the Pacific oceans (~−0.03 permil).

During the first part of the glaciation, surface $\delta^{13}C_{DIC}$ and $\delta^{13}CO_2$ slightly increase due to the slower remineralization rate. The reduced export production leads to a reduced burial of isotopically depleted organic carbon and thus to an increase in the oceanic $\delta^{13}C_{DIC}$. After 50 ka B.P. the weaker export production effect becomes dominant and surface ocean $\delta^{13}C_{DIC}$ as well as $\delta^{13}CO_2$ decrease by about 0.04 permil between 50 and 20 ka B.P. in REM compared to FE (Fig. 4h). During the glaciation deep (≥3000 m) $\delta^{13}C_{DIC}$ decreases by 0.03 permil in experiment REM compared to FE (Fig. 10g).

During the deglaciation both deep $\delta^{13}C_{DIC}$ and $\delta^{13}CO_2$ further decrease by respectively 0.06 and 0.054 permil compared to FE because the export production increases and the nutrient utilisation decreases back to its original value.

6.2.2. Brine parametrization

The greater stratification induced by the brine parametrization implementation leads to a negative $\delta^{13}C_{DIC}$ anomaly at depth (≥3000 m) and a positive $\delta^{13}C_{DIC}$ anomaly at intermediate depth (200–2000 m). Deep $\delta^{13}C_{DIC}$ decreases significantly at 110 ka B.P. (−0.13 permil) and 70 ka B.P. (−0.1 permil) to reach a minimum of −0.24 permil at 40 ka B.P. Surface $\delta^{13}C_{DIC}$ and atmospheric $\delta^{13}CO_2$ first increase slightly (+0.05 permil) as a result of the $\delta^{13}C_{DIC}$ redistribution. However, the weaker export production in experiment BR than in experiment FE leads to a surface $\delta^{13}C_{DIC}$ decrease, which becomes dominant after 40 ka B.P. It also induces less burial of isotopically-depleted organic carbon and therefore leads to a negative long-term trend in the oceanic $\delta^{13}C_{DIC}$. This underlying long-term trend is emerging in the atmosphere and the surface ocean after 40 ka B.P. when export production and nutrient utilisation relax back towards their initial 125 ka B.P. values. At the LGM, deep $\delta^{13}C_{DIC}$ is thus 0.12 permil lower in experiment BR than FE (Fig. 10i), surface $\delta^{13}C_{DIC}$ is 0.08 permil lower and atmospheric $\delta^{13}CO_2$ is 0.1 permil lower (Fig. 4j).

6.2.3. Increase in oceanic phosphate inventory and aeolian iron input

As organic matter is strongly depleted in ^{13}C, a more efficient nutrient utilisation leads to a relative increase in ocean's surface $\delta^{13}C_{DIC}$ and thus to an atmospheric $\delta^{13}CO_2$ increase. Both an increase in oceanic phosphate inventory and aeolian iron input lead to greater export production. As a result, the greater oceanic phosphate inventory and aeolian iron input respectively lead to a 0.4 permil and 0.12 permil increase in atmospheric $\delta^{13}CO_2$ at the LGM (Fig. 4d,l).

However, while aeolian iron input does not lead to any significant change in deep $\delta^{13}C_{DIC}$, a greater oceanic phosphate inventory induces a 0.2 permil increase in deep $\delta^{13}C_{DIC}$ (Fig. 10c,k). In experiment PO, the burial of organic matter increases by 19% compared to experiment FE. The removal of low 13C organic matter from the system is thus responsible for the deep $\delta^{13}C_{DIC}$ increase.

6.2.4. Land carbon reservoir changes

The release (uptake) of carbon with a δC signature of about −23 permil tends to decrease (increase) atmospheric $\delta^{13}CO_2$ and oceanic $\delta^{13}C_{DIC}$. In experiment VG, atmospheric $\delta^{13}CO_2$ and deep $\delta^{13}C_{DIC}$ decrease by respectively 0.1 and 0.08 permil during the period 125–20 ka B.P. and increase by respectively 0.2 and 0.18 permil during the deglaciation (Figs. 4f and 10e) in experiment VG compared to experiment FE. This is in general agreement with proxy-based estimates (Curry et al., 1988; Duplessy et al., 1988; Bird et al., 1994).

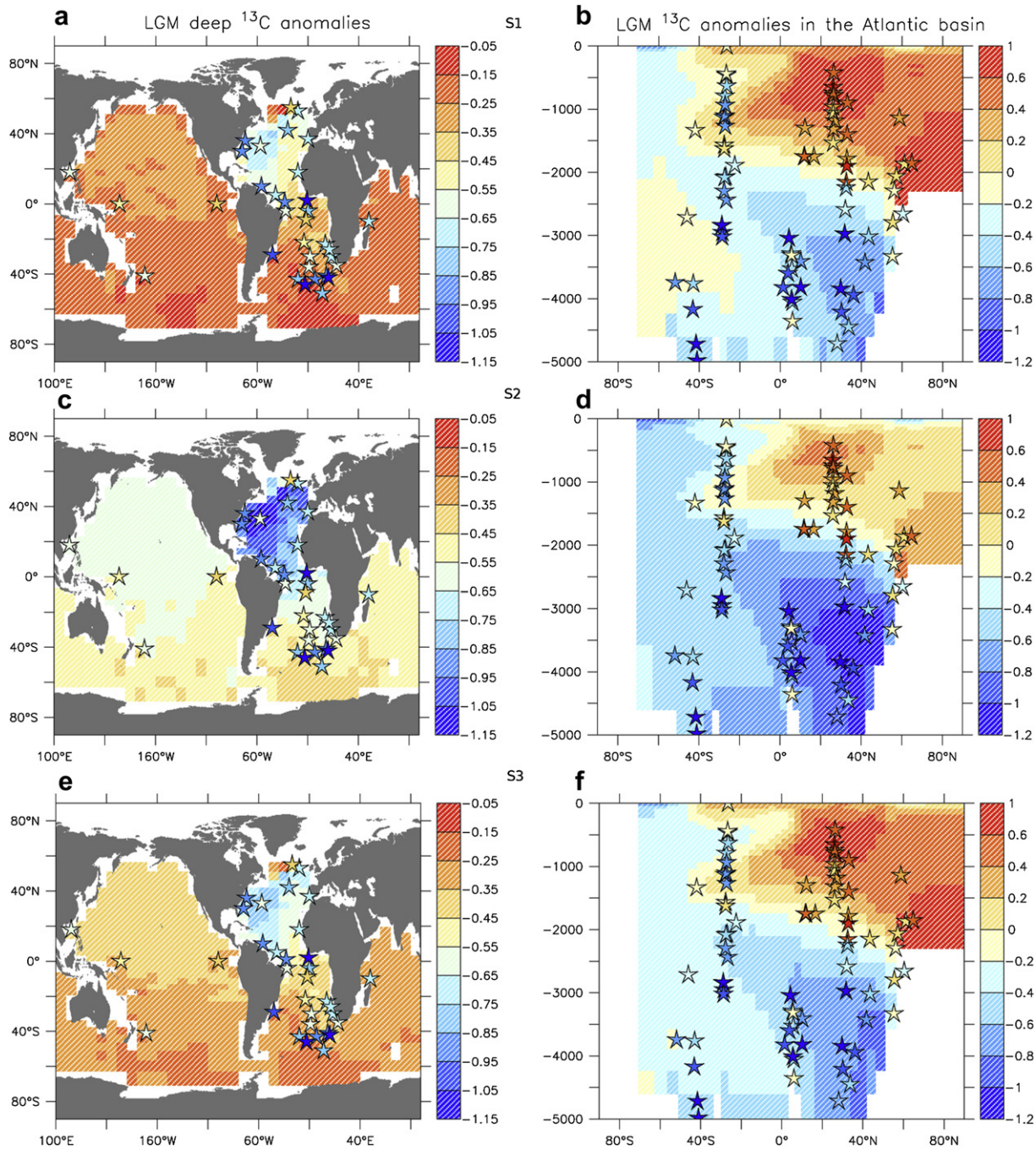

Fig. 9. (left) Deep (2500–5000 m) $\delta^{13}C$ anomalies (permil) at the LGM (20–0 ka B.P.) for experiment $S1_{(Rem,P)}$ (a), $S2_{(Rem,Br)}$ (c) and $S3_{(Br,P)}$ (e). Overlaid are $\delta^{13}C$ LGM anomaly estimates from marine sediment cores (from West to East and North to South) SO50-31KL (Wei et al., 2006), MW91-9 GGC48 (Yu et al., 2010), CHAT10K, ODP1123, CHAT1K, CHAT5K and CHAT3K (McCave et al., 2008), RC13-110 (Mix et al., 1991), KNR 73-3/4 (Boyle and Keigwin, 1985), BOFS 8K (Yu et al., 2010), M17049 (Sarnthein et al., 1994), CHN82-24 (Boyle and Keigwin, 1985), MD99-2334K (Skinner and Shackleton, 2004), MD95-2042 (Pailler and Bard, 2002), KNR 140 (Keigwin, 2004), V30-49 (Mix and Fairbanks, 1985), KNR 110-66, KNR 110-71, KNR 110-75 (Curry et al., 1988), GeoB-4403, GeoB-1520 (Bickert and Mackensen, 2004), GeoB-1523 (Mulitza, 1998), GeoB-1101, GeoB-1105, GeoB-1115, GeoB-1118, GeoB-1112, GeoB-1041, GeoB-1034, GeoB-1035 (Bickert and Wefer, 1996), GeoB-1501, GeoB-1903 (Dürkop et al., 1997), GeoB-5115, GeoB-3801, GeoB-2004, GeoB-3603, GeoB-2019 (Bickert and Mackensen, 2004), GeoB-1214, GeoB-1710 (Schmiedl and Mackensen, 1997), GeoB-1721, GeoB-1722 (Mollenhauer et al., 2002), RC13-229 (Oppo and Fairbanks, 1987), TN057-21, PS20-82, TN057-15 (Ninnemann and Charles, 2002), RC11-83 (Charles et al., 1996), RC15-93, RC15-94, V22-108 (Charles et al., 1991), ODP 1090, ODP 1089 (Hodell et al., 2003) and WIND28K (Yu et al., 2010). (right) $\delta^{13}C$ anomalies (20–0 ka B.P.) averaged over the Atlantic basin as simulated in experiment $S1_{(Rem,P)}$ (b), $S2_{(Rem,Br)}$ (d) and $S3_{(Br,P)}$ (f) compared to the benthic $\delta^{13}C$ anomalies of Curry and Oppo (2005).

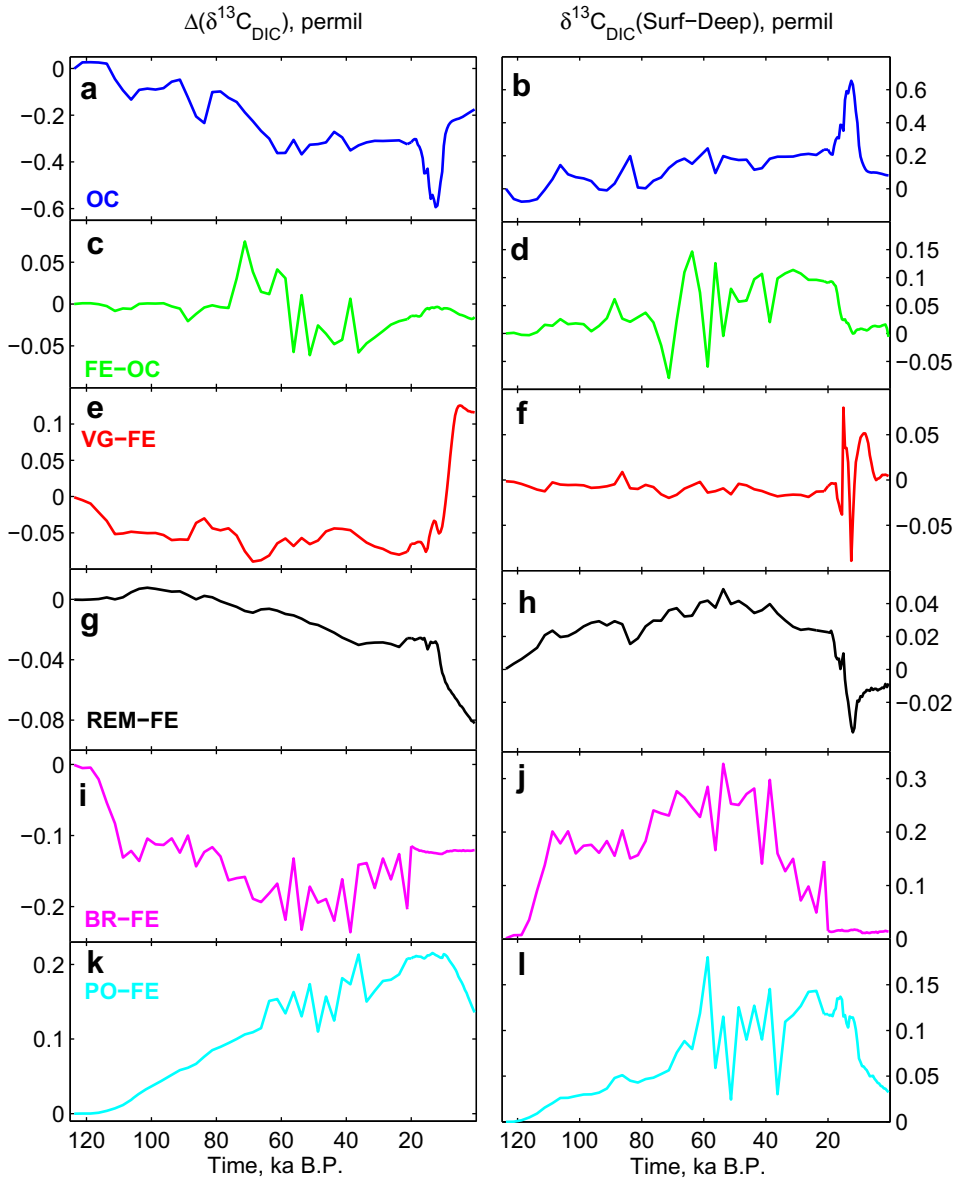

Fig. 10. Time series of globally averaged (left) deep $\delta^{13}C_{DIC}$ and (right) surface to deep $\delta^{13}C_{DIC}$ gradient ($\delta^{13}C$ (Surface)−$\delta^{13}C$ (deep)) for OC (a,b), FE−OC (c,d), VG−FE (e,f), REM−FE (g,h), BR−FE (i,j) and PO−FE (k,l).

Additional experiments performed with a different land carbon forcing (not shown) can provide useful information on the sensitivity of the system to G–IG terrestrial carbon change. A land carbon release of 200 GtC instead of 340 GtC during the period 125–20 ka B.P. would lead to an atmospheric CO_2 increase of 9 ppmv instead of 13 ppmv and to an oceanic $\delta^{13}C_{DIC}$ decrease of 0.3 permil instead of 0.34 permil. On the other hand a land carbon release of 660 GtC would lead to an atmospheric CO_2 increase of 20 ppmv and to an oceanic $\delta^{13}C_{DIC}$ decrease of 0.4 permil.

6.2.5. *Changes in ocean circulation*

The progressive weakening of the AMOC during the glaciation has a non-negligible effect on atmospheric $\delta^{13}CO_2$, which decreases by 0.2 permil in experiment OC (Fig. 4b). However, when experiment OC is performed without a sediment module, the LGM $\delta^{13}CO_2$ is equivalent to the pre-industrial one. This is mainly due to the greater denitrification rates in the deep North Atlantic and the deep North Pacific, which induce a lower organic carbon burial and thus a $\delta^{13}C_{DIC}$ decrease during glacial times (Fig. 10a).

The results of these factorial experiments highlight the intricate evolution of CO_2 and δC in different reservoirs and of the interplay of slowly and relatively fast responding components of the Earth system. This points to the importance of considering spatio-temporal changes over glacial–interglacial cycles both in a dynamic and 3-dimensionally resolved setting.

7. Discussion and conclusions

In this study we explore the impact on atmospheric CO_2, $\delta^{13}CO_2$ and the marine carbon cycle of transient changes in physical and biochemical forcings across a full glacial–interglacial cycle. We applied a model of intermediate complexity that resolves the pattern of change in $\delta^{13}C_{DIC}$, carbonate ion concentration as well as export production of organic matter, calcite and opal in a dynamic 3-dimensional setting. Factorial experiments reveal the

characteristic spatial and temporal response pattern in various proxies for a range of mechanisms (e.g. Figs. 4 and 5). The results illustrate that the spatial patterns of change provide additional constraints on the glacial–interglacial CO_2 problem, which can not be obtained with box or 2-dimensional models. We show that system time lags associated with the slow response time scales of ocean–sediment interactions and the weathering/burial cycle lead to significant memory effects on glacial–interglacial time scales. The intricate interplay of fast and slow response mechanisms complicates the interpretation of proxy records and calls for the consideration of the full spatial and temporal proxy evolution.

About one third of the atmospheric CO_2 decrease from the Eemian to the LGM can be explained by relatively well-established forcings such as temperature, salinity, ocean circulation, aeolian iron input and land carbon inventory changes. The challenge thus remains to explain the other two thirds of the CO_2 change. Here we investigate changes in the remineralization depth of organic material, brine parametrization and changes in oceanic phosphate inventory as possible additional mechanisms. Relative small changes in these forcings lead to significant variations in atmospheric CO_2 in agreement with previous studies (Matsumoto, 2007; Matsumoto et al., 2007; Kwon et al., 2009; Bouttes et al., 2010; Tschumi et al., 2011). However the magnitude and timing of the changes in these forcings bear high uncertainties. When including these forcings in different combinations atmospheric CO_2 decreases by 72–112 ppmv (S1–3, Table 2) during the glaciation, however the deglaciation increase is much reduced (26–50 ppmv). These amplitude differences are partly due to memory effects associated with the long response time scales of ocean–sediment interactions and the weathering–burial cycle (Goodwin and Ridgwell, 2010; Tschumi et al., 2011). Changes in deep $[CO_3^{2-}]$ play an important role in dampening the pCO_2 change. The state of the deep $[CO_3^{2-}]$ at the beginning of the experiment is partly controlling the magnitude of the pCO_2 change: a greater ($\sim$+10 μmol/L) deep $[CO_3^{2-}]$ leads to a $\sim$25% reduction in the atmospheric CO_2 decrease during the glaciation.

There are potential implications of these memory effects. (i) The evaluation of mechanisms based on equilibrium time slice simulations may be hampered by transient, non-equilibrium effects and/or the neglect of ocean–sediment interactions and the weathering–burial cycle. (ii) Atmospheric CO_2 is recorded to decrease several millennia after Antarctic temperature at the Last Glacial inception. One might speculate that this decoupling of CO_2 and Antarctic temperature is related to disequilibrium effects and that the carbon system during the Eemian and the inception was not yet fully adjusted to the previous changes in environmental conditions over the penultimate glacial–interglacial transition. (iii) The mechanisms involved in decreasing CO_2 during the glaciation could partly differ from the ones responsible for the CO_2 increase during the deglaciation. While millennial-scale variability does not seem to play a significant role in decreasing CO_2 between 125 and 20 ka B.P., it could be instrumental in increasing CO_2 between 20 and 10 ka B.P. A better ventilation of the Southern Ocean during H1 could potentially release carbon stored in the deep during the glaciation.

For the brine parametrization, another part of the glacial/deglacial pCO_2 asymmetry is due to the forcing. The time evolution of the pCO_2 in the brine rejection parametrization experiment is set following the ice sheet modelling study of Pollard and DeConto (2009) which suggests that the maximum extent of the West Antarctic ice sheet was almost reached at about 40 ka B.P. Then, both the Weddell and Ross Sea areas were almost completely covered by grounded ice (Bentley and Anderson, 1998; Anderson et al., 2002; Denton and Hughes, 2002) and AABW formation was displaced into the open ocean, where a sinking of very salty waters is highly unlikely to sustain. Formation of Antarctic Bottom Water and brine rejection in the Southern Ocean should be further studied so as to better predict their time evolution during the glaciation.

Finally, the asymmetry observed in the experiments forced with changes in oceanic phosphate inventory is also due to the relatively long ($\sim$20 ka) residence time of phosphorus in the ocean. In addition changes in oceanic phosphate inventory should follow sea level change, which is a relatively late player in the deglaciation. It should be noted that in experiments $S1_{(Rem,P)}$, $S3_{(Br,P)}$ and PO, the potential changes in DIC, alkalinity, silicate and iron induced by the lowered sea level were not taken into account. Ushie and Matsumoto (2012) suggested that the associated input of DIC with phosphate coming from the shelves could offset the pCO_2 drawdown. However any phosphate and DIC inputs from the shelves would also be associated with an alkalinity input, which could mitigate the DIC effect on pCO_2. For example, a similar experiment to PO with inputs of DIC/ALK/P following the ratio 117/117/1 leads to a pCO_2 decrease of 80 ppmv instead of 90 ppmv.

When comparing the results of the S1–3 experiments with paleo-proxies we find that only simulations including an increase in oceanic phosphate inventory ($S1_{(Rem,P)}$ and $S3_{(Br,P)}$) manage to successfully simulate the long-term increase in $\delta^{13}CO_2$ from the Eemian to the LGM (Schneider, 2011) (Fig. 3). In our experiments, iron fertilization is not sufficient to increase $\delta^{13}CO_2$ during the glaciation. In addition, paleo-proxies support a similar or slightly enhanced export production at the LGM compared to pre-industrial times, as it is simulated in experiments forced with a greater oceanic phosphate content ($S1_{(Rem,P)}$, $S3_{(Br,P)}$) (Fig. 5). Simulations S1–3 display an increase in deep $[CO_3^{2-}]$ and a deepening of the calcite saturation horizon. Notably an increase in oceanic phosphate inventory and a deepening of the remineralization depth are the main drivers of deep $[CO_3^{2-}]$ increase. Due to sparse paleo-proxies, it is difficult to conclude but experiment $S1_{(Rem,P)}$ could display a too large deepening of the Pacific calcite saturation horizon (Zeebe and T.M. Marchitto, 2010). Regarding $\delta^{13}C_{DIC}$, simulation $S3_{(Br,P)}$ probably leads to the best representation of both the LGM spatial distribution and the time changes during the glaciation. However, none of the S1–3 simulations display the strong negative $\delta^{13}C_{DIC}$ anomaly observed in the deep South Atlantic at the LGM (Ninnemann and Charles, 2002; Hodell et al., 2003), nor a salinity anomaly of about 2 in the deep Southern Ocean (Adkins et al., 2002). This would suggest that, even when including the brine rejection parametrization, the simulated glacial ocean is not sufficiently stratified. Additional proxies of deep $[CO_3^{2-}]$ change and deep $\delta^{13}C_{DIC}$ are needed in the Pacific basin to gain better confidence on the time evolution and spatial variability of these variables during the glaciation.

Experiments $S1_{(Rem,P)}$ and $S2_{(Rem,Br)}$ show that changes in remineralization depth could have played a role in the atmospheric CO_2 decrease during the glaciation. However, as it has a negative contribution on export production, it had to be associated with a factor enhancing surface nutrient utilisation. The response of our model to iron fertilization could be underestimated, but the results of our experiments also suggest that an increase in nutrient availability at the ocean's surface could be an important contributor to the deglacial pCO_2 decrease. The main problem with a change in oceanic phosphate inventory is the long residence time of phosphorus in the ocean and its strong coupling to sediment processes. The residence time of nitrogen in the ocean being much shorter ($\sim$2000 years), changes in the oceanic nitrogen cycle during the glaciation should be considered seriously (Falkowski, 1997).

As usual, caveats apply to our model and analysis: the wind field was kept constant in all the experiments. A weakening of the southern hemispheric westerlies has been suggested to cause low glacial atmospheric CO_2 (Toggweiler et al., 2006). However, idealised experiments showed that moderate changes ($\leq$50%) in the

westerlies would not lead to significant variations in atmospheric CO_2 (Tschumi et al., 2008; Menviel et al., 2008a; D'Orgeville et al., 2010). In addition, there is currently no consensus as to whether the southern hemispheric westerlies were weaker or not during glacial times (Rojas et al., 2009). Furthermore, Timmermann et al. (submitted for publication) and Varma et al. (2011) recently suggested that the Southern Hemispheric westerlies were strengthening with the Meridional temperature gradient in the Southern hemisphere. The transient simulation of the last 125 ka performed with LOVECLIM (Timmermann et al., submitted for publication) nicely shows that Southern Hemispheric westerlies are stronger at times of low obliquity (20–35 ka B.P. and 60–80 ka B.P.). In brief, the evidence does not support a significant influence of Southern Hemispheric westerlies on glacial–interglacial CO_2.

Changes in chemical weathering, riverine influx, coastal zone processes, Redfield ratios (Omta et al., 2006; Tagliabue et al., 2009) and variations in volcanic CO_2 outgassing (Huybers and Langmuir, 2009; Roth and Joos, 2012) were not taken into account in this study. Cold and dry conditions during glacial times reduce the rate of chemical weathering while increasing the rate of physical weathering. In addition carbonate weathering was increased on exposed shelves due to the lower sea level. The net balance of these changes is very uncertain (Munhoven, 2002; Foster and Vance, 2006; Vance et al., 2009): silicate weathering was most likely slightly greater during interglacial times but its maximum could occur in the early deglaciation during the retreat of the ice sheets (Vance et al., 2009), while carbonate weathering was stable on glacial–interglacial time scales or slightly greater during glacial times (Munhoven, 2002). Given the uncertainties associated with the timing, direction and amplitude of the weathering changes, we preferred not to include them.

Acknowledgement

We thank H. Fischer as well as two anonymous reviewers and the Editor, Claude Hillaire-Marcel, for their helpful comments. This study received support by the Swiss National Science Foundation and by the European Commission through the FP7 projects Past4-Future (grant no. 243908) and CARBOCHANGE (grant no. 264879). L. Menviel was supported by funding from the Oeschger Center for Climate Change Research and is now a research associate at UNSW.

Appendix

Appendix A. Parametrization of the brine rejection variations

The fraction (*frac*) of the salt and geochemical variables transported to depth is set to vary between 0 and 0.4 in agreement with previous study (Bouttes et al., 2011). For the period 125–40 ka B.P., $frac = -0.0414*TA + 0.0244$. For the period 40–23 ka B.P., $frac = 0.115*TA + 1.1925$. TA represents the Antarctic temperature anomaly (°C) as recorded in EPICA Dome C ice core (Jouzel et al., 2007). *frac* is equal to 0 from 21 to 0 ka B.P., and is linearly interpolated between 23 and 21 ka B.P.

Appendix B. Attribution of the pCO_2 changes to physical mechanisms

In addition, to the experiments detailed in Table 1, we performed the following simulations to further attribute simulated changes to mechanisms: experiment TS but with pre-industrial SST (TS-nT), experiment TS without sediment module (TS-nSed) and experiment TS with pre-industrial SST and without sediment module (TS-nT-nSed). We therefore have five experiments (TS, OC, TS-nT, TS-nSed and TS-nT-nSed) and five unknown (effect on pCO_2 of circulation, SST, SSS, export production and sediment). We assume a linear response associated with all the unknowns. Finally, to deconvolute the effect of sea ice on atmospheric CO_2, two additional experiments were performed in which the marine export production and the air–sea CO_2 transfer were not affected by the varying sea ice.

References

Adkins, J., McIntyre, K., Schrag, D., 2002. The salinity, temperature, and $\delta^{18}O$ of the glacial deep ocean. Science 298, 1769–1773.
Ahn, J., Brook, E., 2007. Atmospheric CO_2 and climate from 65 to 30 ka B.P. Geophys. Res. Lett. 34. http://dx.doi.org/10.1029/2007GL029551
Ahn, J., Brook, E., 2008. Atmospheric CO_2 and climate on millennial time scales during the Last Glacial period. Science 322. http://dx.doi.org/10.1126/science.1160832.
Allen, C., Pike, J., Pudsey, C., 2011. Last Glacial–Interglacial sea-ice cover in the SW Atlantic and its potential role in global deglaciation. Quat. Sci. Rev. 30, 2446–2458.
Anderson, J., Shipp, S., Lowe, A., Wellner, J.S., Mosola, A., 2002. The Antarctic Ice Sheet during the Last Glacial Maximum and its subsequent retreat history: a review. Quat. Sci. Rev. 21, 49–70.
Anderson, R.F., Ali, S., Bradtmiller, L., Nielsen, S., Fleisher, M., Anderson, B., Burckle, L., 2009. Wind-driven upwelling in the Southern Ocean and the deglacial rise in atmospheric CO_2. Science 323, 1443–1448.
Archer, D., Winguth, A., Lea, D., Mahowald, N., 2000. What caused the glacial/interglacial atmospheric pCO_2 cycles? Rev. Geophys. 38, 159–189.
Archer, D., Martin, P., Milovich, J., Brovkin, V., Plattner, G., Ashendel, C., 2003. Model sensitivity in the effect of Antarctic sea ice and stratification on atmospheric pCO_2. Paleoceanography 18.
Bacastow, R., Maier-Reimer, E., 1990. Ocean-circulation model of the carbon cycle. Clim. Dyn. 4, 95–125.
Beerling, D., 1999. New estimates of carbon transfer to terrestrial ecosystems between the Last Glacial Maximum and the Holocene. Terra Nova 11, 162–167.
Bendtsen, J., Lundsgaard, C., Middelboe, M., 2002. Influence of bacterial uptake on deep-ocean dissolved organic carbon. Global Biogeochem. Cycles 16. http://dx.doi.org/10.1029/2002GB001947.
Bentley, M., Anderson, J., 1998. Glacial and marine geological evidence for the ice sheet configuration in the Weddell Sea–Antarctic Peninsula region during the Last Glacial Maximum. Antarct. Sci. 10, 309–325.
Berelson, W., 2001. The flux of particulate organic carbon into the ocean interior: a comparison of four U.S. JGOFS regional studies. Oceanography 14, 59–67.
Berger, A., 1978. Long term variations of daily insolation and Quaternary climate change. J. Atmos. Sci. 35, 2362–2367.
Bickert, T., Mackensen, A., 2004. Last Glacial to Holocene changes in South Atlantic deep water circulation. In: Wefer, G., Mulitza, S., Rathmeyer, V. (Eds.), The South Atlantic during the Late Quaternary. Springer, Berlin, pp. 671–695.
Bickert, T., Wefer, G., 1996. Late Quaternary deep-water circulation in the South Atlantic: Reconstruction from carbonate dissolution and benthic stable isotopes. In: Berger, W.H., Wefer, G., Siedler, G. (Eds.), "The South Atlantic: Present and Past Circulation". Springer, pp. 599–620.
Biermann, A., Engel, A., 2010. Effect of CO_2 on the properties and sinking velocity of aggregates of the coccolithophore *Emiliania huxleyi*. Biogeosciences 7, 1017–1029.
Bird, M., Lloyd, J., Farquhar, G., 1994. Terrestrial carbon storage at the LGM. Nature 371, 566.
Bopp, L., Kohfeld, K., Quërë, C.L., Aumont, O., 2003. Dust impact on marine biota and atmospheric CO_2 during glacial periods. Paleoceanography 18. http://dx.doi.org/10.1029/2002PA000810.
Bouttes, N., Paillard, D., Roche, D., 2010. Impact of brine-induced stratification on the glacial carbon cycle. Clim. Past 6. http://dx.doi.org/10.5194/cp–6–575–2010.
Bouttes, N., Paillard, D., Roche, D., Brovkin, V., Bopp, L., 2011. Last Glacial Maximum CO_2 and $\delta^{13}C$ successfully reconciled. Geophys. Res. Lett. 38. http://dx.doi.org/10.1029/2010GL044499
Boyle, E., Keigwin, L., 1985. Comparison of Atlantic and Pacific paleochemical records for the last 215,000 years: changes in deep ocean circulation and chemical inventories. Earth Planet. Sci. Lett. 76, 135–150.
Boyle, E., Keigwin, L., 1987. North Atlantic thermohaline circulation during the past 20,000 years linked to high-latitude surface temperature. Nature 330, 35–40.
Broecker, W., Peng, T.-H., 1986. Glacial to interglacial changes in the operation of the global carbon cycle. Radiocarbon 28, 309–327.
Broecker, W., Peng, T.-H., 1987. The role of $CaCO_3$ compensation in the glacial to interglacial atmospheric CO_2 change. Global Biogeochem. Cycles 1, 15–39.
Broecker, W., 1982. Glacial to Interglacial changes in ocean chemistry. Prog. Oceanogr. 11, 151–197.
Brovkin, V., Ganopolski, A., Archer, D., Rahmstorf, S., 2007. Lowering of glacial atmospheric CO_2 in response to changes in oceanic circulation and marine biogeochemistry. Paleoceanography 22. http://dx.doi.org/10.1029/2006PA001380.
Brovkin, V., Ganopolski, A., Archer, D., Munhoven, G., 2012. Glacial CO_2 cycle as a succession of key physical and biogeochemical processes. Clim. Past 8. http://dx.doi.org/10.5194/cp-8-251-2012.
Buesseler, K., Lamborg, C., Boyd, P., Lam, P., Trull, T., Bidigare, R., Bishop, J., Casciotti, K., Dehairs, F., Elskens, M., Honda, M., Karl, D., Siegel, D., Silver, M.,

Steinberg, D., Valdes, J., Mooy, B.V., Wilson, S., 2007. Revisiting carbon flux through the oceans twilight zone. Science 316, 567–570.
Burke, A., Robinson, L., 2012. The Southern Ocean's role in carbon exchange during the last deglaciation. Science 335, 557–561.
Carlson, G., Hansell, D., Nelson, N., Siegel, D., Smethie, W., Khatiwala, S., Meyers, M., Halewood, E., 2010. Dissolved organic carbon export and subsequent remineralization in the mesopelagic and bathypelagic realms of the North Atlantic basin. Deep Sea Res. II 57, 1433–1445.
Charles, C., Froelich, P., Zibello, M., Mortlock, R., Morley, J., 1991. Biogenic opal in southern ocean sediments over the last 450,000 years: Implications from surface water chemistry and circulation. Paleoceanography 6, 697–728.
Charles, C., Lynch-Stieglitz, J., Ninnemann, U., Fairbanks, R., 1996. Climate connections between the hemispheres revealed by deep sea sediment core/ice core correlations. Earth Planet. Sci. Lett. 142, 19–27.
Chikamoto, M., Abe-Ouchi, A., Oka, A., Ohgaito, R., Timmermann, A., 2012. Quantifying the ocean's role in glacial CO_2 reductions. Clim. Past 8, 545–563.
Ciais, P., Tagliabue, A., Cuntz, M., Bopp, L., Scholze, M., Hoffmann, G., Lourantou, A., Harrison, S., Prentice, I., Kelley, D., Koven, C., Piao, S., 2011. Large inert carbon pool in the terrestrial biosphere during the Last Glacial Maximum. Nat. Geosci.. http://dx.doi.org/10.1038/NGE01324
Colman, A., Holland, H., 2000. The global diagenetic flux of phosphorus from marine sediments to the oceans; redox sensitivity and the control of atmospheric oxygen levels. Soc. Sediment. Geol. Spec. Publ. 66, 53–75.
Curry, W., Oppo, D., 2005. Glacial water mass geometry and the distribution of $\delta^{13}C$ of $\sum CO_2$ in the western Atlantic Ocean. Paleoceanography 20.
Curry, W., Duplessy, J., Labeyrie, L., Shackleton, N., 1988. Changes in the distribution of $\delta^{13}C$ of deep water $\sum CO_2$ between the last glaciation and the Holocene. Paleoceanography 3, 317–341.
D'Orgeville, M., Sijp, W., England, M., Meissner, K., 2010. On the control of glacial–interglacial atmospheric CO_2 variations by the Southern Hemisphere westerlies. Geophys. Res. Lett. 37. http://dx.doi.org/10.1029/2010GL045261
de Boer, A., Watson, A., Edwards, N., Oliver, K., 2010. A multi-variable box model approach to the soft tissue carbon pump. Clim. Past 6, 827–841.
de Vernal, A., Hillaire-Marcel, C., 2000. Sea-ice cover, sea-surface salinity and halo-/thermocline structure of the northwest North Atlantic: modern versus full glacial conditions. Quat. Sci. Rev. 19, 65–85.
de Vernal, A., Eynaud, F., Henry, M., Hillaire-Marcel, C., Londeix, L., Mangin, S., Matthiessen, J., Marret, F., Radi, T., Rochon, A., Solignac, S., Turon, J.-L., 2005. The Northern Hemisphere during the Last Glacial Maximum based on dinoflagellate cyst assemblages. Quat. Sci. Rev. 24, 897–924.
Denton, G., Hughes, T., 2002. Reconstructing the Antarctic Ice Sheet at the Last Glacial Maximum. Quat. Sci. Rev. 21, 193–202.
Doney, S., Glover, D., Najjar, R., 1996. A new coupled, one-dimensional biological-physical model for the upper ocean: applications to the JGOFS Bermuda Atlantic Time-series study (BATS) site 1. Deep Sea Res. Part II 43, 591–624.
Duplessy, J., Shackleton, N., Fairbanks, R., Labeyrie, L., Oppo, D., Kallel, N., 1988. Deepwater source variations during the last climate cycle and their impact on the global deepwater circulation. Paleoceanography 3, 343–360.
Dürkop, A., Hale, W., Mulitza, S., PLtzold, J., Wefer, G., 1997. Late Quaternary variations of sea surface salinity and temperature in the western tropical Atlantic: evidence from $\delta^{18}O$ of *Globigerinoides sacculifer*. Paleoceanography 12, 764–772.
Edwards, N., Marsh, R., 2005. Uncertainties due to transport-parameter sensitivity in an efficient 3-D ocean-climate model. Clim. Dyn. 3, 67–94.
Edwards, N., Willmott, A., Killworth, P., 1998. On the role of topography and wind stress on the stability of the thermohaline circulation. J. Phys. Oceanogr. 28, 756–778.
Edwards, N., 1975. Effects of temperature and moisture on carbon dioxide evolution in a mixed deciduous forest floor. Soil Sci. Soc. Am. Proc. 39, 361–365.
Elsig, J., Schmitt, J., Leuenberger, D., Schneider, R., Eyer, M., Leuenberger, M., Joos, F., Fischer, H., Stocker, T., 2009. Stable isotope constraints on Holocene carbon cycle changes from an Antarctic ice core. Nature 461, 507–510.
Eppley, R., 1972. Temperature and phytoplankton growth in the sea. Fish. Bull. 70, 1063–1085.
Fairbanks, R., 1989. A 17,000-year glacio-eustatic sea level record: influence of glacial melting rates on the Younger Dryas event and deep-ocean circulation. Nature 342, 637–642.
Falkowski, P., 1997. Evolution of the nitrogen cycle and its influence on the biological sequestration of CO_2 in the ocean. Nature 387, 272–275.
Filippelli, G., Latimer, J., Murray, R., Flores, J.-A., 2007. Productivity records from the Southern Ocean and the equatorial Pacific Ocean: testing the glacial shelf-nutrient hypothesis. Deep-Sea Res. II 54, 2443–2452.
Filippelli, G., 1997. Controls on phosphorus concentration and accumulation in oceanic sediments. Mar. Geol. 139, 231–240.
Foster, G., Vance, D., 2006. Negligible glacial–interglacial variation in continental chemical weathering rates. Nature 444, 918–921.
Francois, R., Altabet, M., Yu, E., Sigman, D., Bacon, M., Frank, M., Bohrmann, G., Bareille, G., Labeyrie, L., 1997. Contribution of Southern Ocean surface-water stratification to low atmospheric CO_2 concentrations during the Last Glacial period. Nature 389, 929–935.
Francois, L., Delire, C., Warnant, P., Munhoven, G., 1998. Modelling the glacial–interglacial changes in the continental biosphere. Global Planet. Change 16-17, 37–52.
Freeman, K., Hayes, J., 1992. Fractionation of carbon isotopes by phytoplankton and estimates of ancient CO_2 levels. Global Biogeochem. Cycles 6, 185–198.
Gehlen, M., Bopp, L., Emprin, N., Aumont, O., Heinze, C., Ragueneau, O., 2006. Reconciling surface ocean productivity, export fluxes and sediment composition in a global biogeochemical ocean model. Biogeosciences 3, 521–537.
Gersonde, R., Crosta, X., Abelmann, A., Armand, L., 2005. Sea-surface temperature and sea ice distribution of the Southern Ocean at the EPILOG Last Glacial Maximum – a circum-Antarctic view based on siliceous microfossil records. Quat. Sci. Rev. 24, 869–896.
Gildor, H., Tziperman, E., 2001. Physical mechanisms behind biogeochemical glacial–interglacial CO_2 variations. Geophys. Res. Lett. 28, 2421–2424.
Gildor, H., Tziperman, E., Toggweiler, J., 2002. Sea ice switch mechanism and glacial–interglacial CO_2 variations. Global Biogeochem. Cycles 16. http://dx.doi.org/10.1029/2001GB001446.
Goodwin, P., Ridgwell, A., 2010. Ocean–atmosphere partitioning of anthropogenic carbon dioxide on multimillennial timescales. Global Biogeochem. Cycles 24. http://dx.doi.org/10.1029/2008GB003449.
Guidry, M., Mackenzie, F., 2003. Experimental study of igneous and sedimentary apatite dissolution: control of pH, distance from equilibrium, and temperature on dissolution rates. Geochim. Cosmochim. Acta 67, 2949–2963.
Heinze, C., Maier-Reimer, E., Winn, K., 1991. Glacial pCO_2 reduction by the world ocean: experiments with the Hamburg Carbon Cycle Model. Paleoceanography 6, 395–430.
Heinze, C., Maier-Reimer, E., Winguth, A., Archer, D., 1999. A global oceanic sediment model for long-term climate studies. Global Biogeochem. Cycles 13, 221–250.
Hodell, D., Venz, K., Charles, C., Ninnemann, U., 2003. Pleistocene vertical carbon isotope and carbonate gradients in the South Atlantic sector of the Southern Ocean. Geochem. Geophys. Geosys. 4, 1004.
Holden, P., Edwards, N., Oliver, K., Lenton, T., Wilkinson, R., 2010a. A probabilistic calibration of climate sensitivity and terrestrial carbon change in GENIE-1. Clim. Dyn. 35, 785–806.
Holden, P., Edwards, N., Wolff, E., Lang, N., Singarayer, J., Valdes, P., Stocker, T., 2010b. Interhemispheric coupling, the West Antarctic Ice Sheet and warm Antarctic interglacials. Clim. Past 6, 431–443.
Hönisch, B., Bickert, T., Hemming, N., 2008. Modern and Pleistocene boron isotope composition of the benthic foraminifer *Cibicidoides wuellerstorfi*. Earth Planet. Sci. Lett. 272, 309–318.
Huybers, P., Langmuir, C., 2009. Feedback between deglaciation, volcanism, and atmospheric CO_2. Earth Planet. Sci. Lett. 286, 479–491.
Indermühle, A., Monnin, E., Stauffer, B., Stocker, T., Wahlen, M., 2000. Atmospheric CO_2 concentration from 60 to 20 kyr BP from the Taylor Dome ice core, Antarctica. Geophys. Res. Lett. 27, 735–738.
Jin, X., Gruber, N., Dunne, J., Sarmiento, J., Armstrong, R., 2006. Diagnosing the contribution of phytoplankton functional groups to the production and export of particulate organic carbon, $CaCO_3$, and opal from global nutrient and alkalinity distributions. Global Biogeochem. Cycles 20. http://dx.doi.org/10.1029/2005GB002532.
Joos, F., Sarmiento, J., Siegenthaler, U., 1991. Estimates of the effect of southern ocean iron fertilization on atmospheric CO_2 concentrations. Nature 349, 772–775.
Joos, F., Gerber, S., Prentice, I., Otto-Bliesner, B., Valdes, P., 2004. Transient simulations of Holocene atmospheric carbon dioxide and terrestrial carbon since the Last Glacial Maximum. Global Biogeochem. Cycles 18. http://dx.doi.org/10.1029/2003GB002156.
Jouzel, J., Masson, V., Cattani, O., Dreyfus, G., Falourd, S., Hoffmann, G., Minster, B., Nouet, J., Barnola, J., Chappellaz, J., Fischer, H., Gallet, J., Leuenberger, S.J.M., Loulergue, L., Luethi, D., Oerter, H., Parrenin, F., Raisbeck, G., Raynaud, D., Schilt, A., Schwander, J., Selmo, E., Souchez, R., Spahni, R., Stauffer, B., Steffenssen, J.P., Stenni, B., Stocker, T., Tison, J., Werner, M., Wolff, E., 2007. Orbital and millennial Antarctic climate variability over the past 800,000 years. Science 317, 793–796.
Kaplan, J., Prentice, I., Knorr, W., Valdes, P., 2002. Modeling the dynamics of the terrestrial carbon storage since the Last Glacial Maximum. Geophys. Res. Lett. 29. http://dx.doi.org/10.1029/2002GL015230
Keigwin, L., 2004. Radiocarbon and stable isotope constraints on Last Glacial Maximum and Younger Dryas ventilation in the western North Atlantic. Paleoceanography 19. http://dx.doi.org/10.1029/2004PA001029.
Klaas, C., Archer, D., 2002. Association of sinking organic matter with various types of mineral ballast in the deep sea: implications for the rain ratio. Global Biogeochem. Cycles 16. http://dx.doi.org/10.1029/2001GB001765.
Kleinen, T., Brovkin, V., von Bloh, W., Archer, D., Munhoven, G., 2010. Holocene carbon cycle dynamics. Geophys. Res. Lett. 37. http://dx.doi.org/10.1029/2009GL041391
Kohfeld, K.E., Ridgwell, A., 2009. Glacial-interglacial variability in atmospheric CO2. In: Le Quéré, C., Saltzman, E. (Eds.), Surface Ocean/Lower Atmosphere Processes, Geophysical Monograph Series 37. American Geophysical Union, Washington, DC.
Kohfeld, K., Quere, C.L., Harrison, S., Anderson, R., 2005. Role of marine biology in glacial–interglacial CO_2 cycles. Science 308, 74–78.
Köhler, P., Fischer, H., 2006. Simulating low frequency changes in atmospheric CO_2 during the last 740 000 years. Clim. Past 2, 57–78.
Köhler, P., Fischer, H., Munhoven, G., Zeebe, R., 2005. Quantitative interpretation of atmospheric carbon records over the Last Glacial termination. Global Biogeochem. Cycles 19. http://dx.doi.org/10.1029/2004GB002345.
Krakauer, N., Randerson, J., Primeau, F., Gruber, N., Menemenlis, D., 2006. Carbon isotope evidence for the latitudinal distribution and wind speed dependence of the air–sea gas transfer velocity. Tellus 58B, 390–417.
Kurahashi-Nakamura, T., Abe-Ouchi, A., Yamanaka, Y., Misumi, K., 2007. Compound effects of Antarctic sea ice on atmospheric pCO_2 change during

glacial–interglacial cycle. Geophys. Res. Lett. 34. http://dx.doi.org/10.1029/2007GL030898
Kwon, E., Primeau, F., Sarmiento, J., 2009. The impact of remineralization depth on the air–sea carbon balance. Nat. Geosci. 2, 630–635.
Lambert, F., Delmonte, B., Petit, J., Bigler, M., Kaufmann, P.R., Hutterli, M., Stocker, T., Ruth, U., Steffensen, J., Maggi, V., 2008. Dust-climate couplings over the past 800,000 years from the EPICA Dome C ice core. Nature 452, 616–619.
Laws, E., Falkowski, P., Smith, W., Ducklow, H., 2000. Temperature effects on export production in the open ocean. Global Biogeochem. Cycles 14, 1231–1246.
Lefevre, N., Watson, A., 1999. Modeling the geochemical cycle of iron in the oceans and its impact on atmospheric CO_2 concentrations. Global Biogeochem. Cycles 13. http://dx.doi.org/10.1029/1999GB900034.
Lisiecki, L.E., Raymo, M.E., 2005. A Pliocene-Pleistocene stack of 57 globally distributed benthic $\delta^{18}O$ records. Paleoceanography 20. http://dx.doi.org/10.1029/2004PA001071.
Lisiecki, L.E., Raymo, M.E., Curry, W., 2008. Atlantic overturning responses to Late Pleistocene climate forcings. Nature 456, 85–88.
Loulergue, L., Schilt, A., Spahni, R., Masson-Delmotte, V., Blunier, T., Lemieux, B., Barnola, J.-M., Raynaud, D., Stocker, T., Chappellaz, J., 2008. Orbital and millennial-scale features of atmospheric CH_4 over the past 800,000 years. Nature 453, 383–386.
Lourantou, A., Lavric, J., Kohler, P., Barnola, J.-M., Paillard, D., Michel, E., Raynaud, D., Chappellaz, J., 2010. Constraint of the CO_2 rise by new atmospheric carbon isotopic measurements during the last deglaciation. Global Biogeochem. Cycles 24. http://dx.doi.org/10.1029/2009GB003545.
Lund, D., Adkins, J., Ferrari, R., 2011. Abyssal Atlantic circulation during the Last Glacial Maximum: constraining the ratio between transport and vertical mixing. Paleoceanography 26. http://dx.doi.org/10.1029/2010PA001938.
Luo, C., Mahowald, N., del Corral, J., 2003. Sensitivity study of meteorological parameters on mineral aerosol mobilization, transport, and distribution. J. Geophys. Res. 108. http://dx.doi.org/10.1029/2003JD003483
Lüthi, D., Floch, M.L., Bereiter, B., Blunier, T., Barnola, J.-M., Siegenthaler, U., Raynaud, D., Jouzel, J., Fischer, H., Kawamura, K., Stocker, T., 2008. High-resolution carbon dioxide concentration record 650,000–800,000 years before present. Nature 453. http://dx.doi.org/10.1038/nature06949.
Mahowald, N., Yoshioka, M., Collins, W., Conley, A., Fillmore, D., Coleman, D., 2006. Climate response and radiative forcing from mineral aerosols during the glacial maximum, pre-industrial, current and doubled-carbon dioxide climates. Geophys. Res. Lett. 33. http://dx.doi.org/10.1029/2006GL026126
Maier-Reimer, E., Kriest, I., Segschneider, J., Wetzel, P., 2005. The Hamburg Ocean Carbon Cycle Model Hamocc5.1. Tech. Rep., Max Planck Institute for Meteorology.
Marchitto, T., Lynch-Stieglitz, J., Hemming, S., 2005. Deep Pacific $CaCO_3$ compensation and glacial–interglacial atmospheric CO_2. Earth Planet. Sci. Lett. 231, 317–336.
Martin, J., Karl, G.A.K.D., Broenkow, W., 1987. VERTEX: carbon cycling in the northeast Pacific. Deep-Sea Res. 34, 267–285.
Martin, P., Lampitt, R., Perry, M., Sanders, R., Lee, C., DAsaro, E., 2011. Export and mesopelagic particle flux during a North Atlantic spring diatom bloom. Deep Sea Res. I 158, 338–349.
Martin, J., 1990. Glacial–interglacial CO_2 change: the iron hypothesis. Paleoceanography 5, 1–13.
Martrat, B., Grimalt, J., Shackleton, N., de Abreu, L., Hutterli, M., Stocker, T., 2007. Four climate cycles of recurring deep and surface water destabilizations on the Iberian margin. Science 317, 502–507.
Matsumoto, K., Hashioka, T., Yamanaka, Y., 2007. Effect of temperature-dependent organic carbon decay on atmospheric pCO_2. J. Geophys. Res. 112. http://dx.doi.org/10.1029/2006JG000187
Matsumoto, K., 2007. Biology-mediated temperature control on atmospheric pCO_2 and ocean biogeochemistry. Geophys. Res. Lett. 34. http://dx.doi.org/10.1029/2007GL031301
McCave, I., Carter, L., Hall, I., 2008. Glacial–interglacial changes in water mass structure and flow in the SW Pacific Ocean. Quat. Sci. Rev. 27, 1886–1908.
McManus, J.F., Francois, R., Gherardi, J.M., Keigwin, L.D., Brown-Leger, S., 2004. Collapse and rapid resumption of Atlantic meridional circulation linked to deglacial climate changes. Nature 428, 834–837.
Menviel, L., Joos, F., 2012. Towards explaining the Holocene carbon dioxide and carbon isotope records: results from transient carbon cycle-climate simulations. Paleoceanography 27. http://dx.doi.org/10.1029/2011PA002224.
Menviel, L., Timmermann, A., Mouchet, A., Timm, O., 2008a. Climate and marine carbon cycle response to changes in the strength of the southern hemispheric westerlies. Paleoceanography 23. http://dx.doi.org/10.1029/2007PA001604.
Menviel, L., Timmermann, A., Mouchet, A., Timm, O., 2008b. Meridional reorganizations of marine and terrestrial productivity during Heinrich events. Paleoceanography 23. http://dx.doi.org/10.1029/2007PA001445.
Menviel, L., Timmermann, A., Timm, O., Mouchet, A., 2011. Deconstructing the Last Glacial Termination: the role of millennial and orbital-scale forcings. Quat. Sci. Rev. 30, 1155–1172.
Middelboe, M., Lundsgaard, C., 2003. Microbial activity in the Greenland Sea: role of DOC lability, mineral nutrients and temperature. Aquat. Microb. Ecol. 32, 151–163.
Mix, A., Fairbanks, R., 1985. North Atlantic surface-ocean control of Pleistocene deep-ocean circulation. Earth Planet. Sci. Lett. 73, 231–243.
Mix, A., Pisias, N., Zahn, R., Rugh, W., Lopez, C., Nelson, K., 1991. Carbon 13 in Pacific deep and intermediate waters, 0–370 ka: implications for ocean circulation and Pleistocene CO_2. Paleoceanography 6, 205–226.
Mollenhauer, G., Schneider, R., Müller, P., Spiess, V., Wefer, G., 2002. Glacial/interglacial variability in the Benguela upwelling system: spatial distribution and budgets of organic carbon accumulation. Global Biogeochem. Cycles 16. http://dx.doi.org/10.1029/2001GB001488.
Montenegro, A., Eby, M., Kaplan, J., Meissner, K., Weaver, A., 2006. Carbon storage on exposed continental shelves during the glacial–interglacial transition. Geophys. Res. Lett. 33. http://dx.doi.org/10.1029/2005GL025480
Mook, W., 1988. ^{13}C in atmospheric CO_2. Neth. J. Sea Res. 20, 211–223.
Mulitza, S., 1998. Stable isotopes of sediment core GeoB1523-2. PANGEA. http://dx.doi.org/10.1594/PANGAEA.54618.
Müller, S., Joos, F., Edwards, N., Stocker, T., 2006. Water mass distribution and ventilation time scales in a cost-efficient three-dimensional ocean model. J. Clim. 19, 5479–5499.
Müller, S., Joos, F., Edwards, N., Stocker, T., 2008. Modeled natural and excess radiocarbon: sensitivities to the gas exchange formulation and ocean transport strength. Global Biogeochem. Cycles 22. http://dx.doi.org/10.1029/2007GB003065.
Munhoven, G., 2002. Glacial–interglacial changes of continental weathering: estimates of the related CO_2 and HCO_3^- flux variations and their uncertainties. Global Planet. Change 33, 155–176.
Najjar, R., Orr, J., Sabine, C., Joos, F., 1999. Biotic-howto. Tech. Rep., LSCE/CEA Saclay, Gif-sur-Yvette, France.
Negre, C., Zahn, R., Thomas, A., Masquë, P., Henderson, G., Martïnez-Mëndez, G., Hall, I., Mas, J., 2010. Reversed flow of Atlantic deep water during the Last Glacial Maximum. Nature 468. http://dx.doi.org/10.1038/nature09508.
Ninnemann, U., Charles, C., 2002. Changes in the mode of Southern Ocean circulation over the last glacial cycle revealed by foraminiferal stable isotopic variability. Earth Planet. Sci. Lett. 201, 383–396.
Oliver, K., Edwards, N., 2008. Location of potential energy sources and the export of dense water from the Atlantic Ocean. Geophys. Res. Lett. 35. http://dx.doi.org/10.1029/2008GL035537
Oliver, K., Hoogakker, B., Crowhurst, S., Henderson, G., Rickaby, R., Edwards, N., Elderfield, H., 2010. A synthesis of marine sediment core $\delta^{13}C$ data over the last 150,000 years. Clim. Past 6, 645–673.
Omta, A., Bruggeman, J., Kooijman, S., Dijkstra, H., 2006. Biological carbon pump revisited: feedback mechanisms between climate and Redfield ratio. Geophys. Res. Lett. 33. http://dx.doi.org/10.1029/2006GL026213
Oppo, D., Fairbanks, R., 1987. Variability in the deep and intermediate water circulation of the Atlantic Ocean during the past 25,000 years: Northern hemisphere modulation of the Southern Ocean. Earth Planet. Sci. Lett. 86, 1–15.
Orr, J., Najjar, R., 1999. Abiotic-howto. Tech. Rep.. LSCE/CEA Saclay, Gif-sur-Yvette, France.
Paillard, D., Parrenin, F., 2004. The Antarctic ice sheet and the triggering of deglaciations. Earth Planet. Sci. Lett. 227, 263–271.
Pailler, D., Bard, E., 2002. High frequency palaeoceanographic changes during the past 140,000 yr recorded by the organic matter in sediments of the Iberian Margin. Palaeogeogr. Palaeoclim. Palaeoecol. 181, 431–452.
Parekh, P., Dutkiewicz, S., Follows, M., Ito, T., 2006a. Atmospheric carbon dioxide in a less dusty world. Geophys. Res. Lett. 33. http://dx.doi.org/10.1029/2005GL025098
Parekh, P., Follows, M., Dutkiewicz, S., Ito, T., 2006b. Physical and biological regulation of the soft tissue carbon pump. Paleoceanography 21. http://dx.doi.org/10.1029/2005PA001258.
Parekh, P., Joos, F., Müller, S., 2008. A modeling assessment of the interplay between aeolian iron fluxes and iron-binding ligands in controlling carbon dioxide fluctuations during Antarctic warm events. Paleoceanography 23. http://dx.doi.org/10.1029/2007PA001531.
Peltier, W., 1994. Ice-age paleotopography. Science 265, 195–201.
Peltier, W., 2004. Global glacial isostasy and the surface of the ice-age Earth: the ICE-5G (VM2) model and GRACE. Annu. Rev. Earth Planet. Sci. 23, 335–357.
Petit, J., Jouzel, J., Raynaud, D., Barkov, N., Barnola, J.-M., Basile, I., Bender, M., Chappellaz, J., Davis, M., Delaygue, G., Delmotte, M., Kotlyakov, V., Legrand, M., Lipenkov, V., Lorius, C., Pepin, L., Ritz, C., Saltzman, E., Stievenard, M., 1999. Climate and atmospheric history of the past 420,000 years from the Vostok ice core, Antarctica. Nature 399, 429–436.
Pflaumann, U., Sarnthein, M., Chapman, M., d'Abreu, L., Funnell, B., Huels, M., Kiefer, T., Maslin, M., Schulz, H., Swallow, J., van Kreveld, S., Vautravers, M., Vogelsang, E., Weinelt, M., 2003. Glacial North Atlantic: sea-surface conditions reconstructed by GLAMAP 2000. Paleoceanography 18.
Piotrowski, A., Goldstein, S., Hemming, S.R., Fairbanks, R., Zylberberg, D., 2008. Oscillating glacial northern and southern deep water formation from combined neodymium and carbon isotopes. Earth Planet. Sci. Lett. 272, 394–405.
Pollard, D., DeConto, R., 2009. Modelling West Antarctic ice sheet growth and collapse through the past five million years. Nature 458, 329–332.
Reimer, P., Baillie, M., Bard, E., Bayliss, A., Beck, J., Blackwell, P., Ramsey, C.B., Buck, C., Burr, G., Edwards, R., Friedrich, M., Grootes, P., Guilderson, T., Hajdas, I., Heaton, T., Hogg, A., Hughen, K., Kaiser, K., Kromer, B., McCormac, F., Manning, S., Reimer, R., Richards, D., Southon, J., Talamo, S., Turney, C., van der Plicht, J., Weyhenmeyer, C., 2009. IntCal09 and Marine09 radiocarbon age calibration curves, 0–50,000 years cal BP. Radiocarbon 51, 1111–1150.
Rickaby, R., Elderfield, H., Roberts, N., Hillenbrand, C.-D., Mackensen, A., 2010. Evidence for elevated alkalinity in the glacial Southern Ocean. Paleoceanography 25. http://dx.doi.org/10.1029/2009PA001762.
Ridgwell, A., Watson, A., Maslin, M., Kaplan, J., 2003. Implication of the coral reef buildup for the controls on atmospheric CO_2 since the Last Glacial Maximum. Paleoceanography 18. http://dx.doi.org/10.1029/2003PA000893.

Ridgwell, A., 2001. Glacial–Interglacial Perturbations in the Global Carbon Cycle. Ph.D. thesis, University of East Anglia, Norwich, UK.
Ritz, S., Stocker, T., Joos, F., 2011. A coupled dynamical ocean – energy balance atmosphere model for paleoclimate studies. J. Clim. 24, 349–375.
Rojas, M., Moreno, P., Kageyama, M., Crucifix, M., Hewitt, C., Abe-Ouchi, A., Ohgaito, R., Brady, E., Hope, P., 2009. The southern westerlies during the Last Glacial Maximum in PMIP2 simulations. Clim. Dyn. 32. http://dx.doi.org/10.1007/s00382–008–0421–7
Roth, R., Joos, F., 2012. A possible role for volcanic carbon emissions in regulating glacial–interglacial CO_2 variations? Earth Planet. Sci. Lett. 329-330, 141–149.
Sanyal, A., Hemming, N., Hanson, G., Broecker, W., 1995. Evidence for a higher pH in the glacial ocean from boron isotopes in foraminifera. Nature 373, 234–236.
Sarnthein, M., Winn, K., Jung, S., Duplessy, J., Labeyrie, L., Erlenkeuser, H., Ganssen, G., 1994. Changes in east Atlantic deep water circulation over the last 30,000 years: eight time slice reconstructions. Paleoceanography 9, 209–269.
Schmiedl, G., Mackensen, A., 1997. Late Quaternary paleoproductivity and deep water circulation in the eastern South Atlantic Ocean: evidence from benthic foraminifera. Palaeogeogr. Palaeoclim. Palaeoecol. 130, 43–80.
Schmitt, J., Schneider, R., Elsig, J., Leuenberger, D., Lourantou, A., Chappellaz, J., Köhler, P., Joos, F., Stocker, T., Leuenberger, M., Fischer, H., 2012. Carbon isotope constraints on the deglacial CO_2 rise from ice cores. Science 136, 711–714.
Schmittner, A., Brook, E., Ahn, J., 2007. Impact of the ocean's overturning circulation on atmospheric CO2 in Ocean Circulation: Mechanisms and Impacts. In: Schmittner, A., Chiang, J., Hemming, S. (Eds.), AGU Geophysical Monograph Series, vol. 173, pp. 209–246, American Geophysical Union. pdf.
Schneider, B., Bopp, L., Gehlen, M., 2008. Assessing the sensitivity of modeled air–sea CO_2 exchange to the remineralization depth of particulate organic and inorganic carbon. Global Biogeochem. Cycles 22. http://dx.doi.org/10.1029/2007GB003100.
Schneider, R., 2011. Quantifying Past Changes of the Global Carbon Cycle Based on $\delta^{13}CO_2$ Measurements in Antarctic Ice Cores. Ph.D. thesis, Department of Climate and Environmental Physics, Physics Department, University of Bern, Switzerland.
Siegenthaler, U., Muennich, K., 1981. SCORE 16: Carbon Cycle Modelling. Wiley, Chichester. Ch. Carbon-13/Carbon-12 Fractionation During Carbon Dioxide Transfer from Air to Sea.
Siegenthaler, U., Oeschger, H., 1987. Biospheric CO_2 emissions during the past 200 years reconstructed by convolution of ice core data. Tellus B 39, 140–154.
Siegenthaler, U., Stocker, T., Monnin, E., Luthi, D., Schwander, J., Stauffer, B., Raynaud, D., Barnola, J., Fischer, H., Masson-Delmotte, V., Jouzel, J., 2005. Stable carbon cycle–climate relationship during the late Pleistocene. Science 310, 1313–1317.
Sigman, D., Boyle, E., 2000. Glacial/interglacial variations in atmospheric carbon dioxide. Nature 407, 859–869.
Sigman, D., McCorkle, D., Martin, W., 1998. The calcite lysocline as a constraint on glacial/interglacial low-latitude production changes. Global Biogeochem. Cycles 12, 409–427.
Six, K., Maier-Reimer, E., 1996. Effects of plankton dynamics on seasonal carbon fluxes in an ocean general circulation model. Global Biogeochem. Cycles 10, 559–583.
Skinner, L., Shackleton, N., 2004. Rapid transient changes in northeast Atlantic deep water ventilation age across Termination I. Paleoceanography 19. http://dx.doi.org/10.1029/2003PA000983.
Spero, H., Lea, D., 2002. The cause of carbon isotope minimum events on glacial termination. Science 296, 522–525.
Steinacher, M., Joos, F., Frolicher, T., Bopp, L., Cadule, P., Cocco, V., Doney, S., Gehlen, M., Lindsay, K., Moore, J., Schneider, B., Segschneider, J., 2010. Projected 21st century decrease in marine productivity: a multi-model analysis. Biogeosciences 7, 979–1005.
Stephens, B., Keeling, R., 2000. The influence of Antarctic sea ice on glacial–interglacial CO_2 variations. Nature 404, 171–174.
Tagliabue, A., Bopp, L., Roche, D., Bouttes, N., Dutay, J.-C., Alkama, R., Kageyama, M., Michel, E., Paillard, D., 2009. Quantifying the roles of ocean circulation and biogeochemistry in governing ocean carbon-13 and atmospheric carbon dioxide at the Last Glacial Maximum. Clim. Past 5, 695–706.
Tamburini, F., Föllmi, K., 2009. Phosphorus burial in the ocean over glacial–interglacial time scales. Biogeosciences 6, 501–513.
Timmermann, A., Friedrich, T., Timm, O.E., Chikamoto, M., Abe-Ouchi, A. Obliquity and CO_2 Effects on Southern Hemispheric Westerlies and Antarctic Temperatures, submitted for publication.
Toggweiler, J., Russell, J., Carson, S., 2006. Midlatitude westerlies, atmospheric CO_2, and climate change during ice ages. Paleoceanography 21. http://dx.doi.org/10.1029/2005PA001154.
Toggweiler, J., 1999. Variation of atmospheric CO_2 by ventilation of the ocean's deepest water. Paleoceanography 14, 571–588.
Tschumi, T., Joos, F., Parekh, P., 2008. How important are Southern Hemisphere wind changes for low glacial carbon dioxide? A model study. Paleoceanography. http://dx.doi.org/10.1029/2008PA001592.
Tschumi, T., Joos, F., Gehlen, M., Heinze, C., 2011. Deep ocean ventilation, carbon isotopes, marine sedimentation and the deglacial CO_2 rise. Clim. Past 7, 771–800.
Ushie, H., Matsumoto, K., 2012. The role of shelf nutrients on glacial–interglacial CO_2: a negative feedback. Global Biogeochem. Cycles 26. http://dx.doi.org/10.1029/2011GB004147.
Vance, D., Teagle, D., Foster, G., 2009. Variable Quaternary chemical weathering fluxes and imbalances in marine geochemical budgets. Nature 458, 493–496.
Varma, V., Prange, M., Merkel, U., Kleinen, T., Lohmann, G., Pfeiffer, M., Renssen, H., Wagner, A., Wagner, S., Schulz, M., 2011. Holocene evolution of the Southern Hemisphere westerly winds in transient simulations with global climate models. Clim. Past Disc. 7, 1797–1824.
Vecsei, A., Berger, W., 2004. Increase of atmospheric CO_2 during deglaciation: constraints on the coral reef hypothesis from patterns of deposition. Global Biogeochem. Cycles 18. http://dx.doi.org/10.1029/2003GB002147.
Waelbroeck, C., Paul, A., Kucera, M., Rosell-Mel, A., Weinelt, M., Schneider, R., Mix, A., Abelmann, A., Armand, L., Bard, E., Barker, S., Barrows, T., Benway, H., Cacho, I., Chen, M., Cortijo, E., Crosta, X., de Vernal, A., Dokken, T., Duprat, J., Elderfield, H., Eynaud, F., Gersonde, G., Hayes, A., Henry, M., Hillaire-Marcel, C., Huang, C., Jansen, E., Juggins, S., Kallel, N., Kiefer, T., Kienast, M., Labeyrie, L., Leclaire, H., Londeix, L., Mangin, S., Matthiessen, J., Marret, F., Meland, M., Morey, A., Mulitza, S., Pflaumann, U., Pisias, N., Radi, T., Rochon, A., Rohling, E., Sbaffi, L., Schfer-Neth, C., Solignac, S., Spero, H., Tachikawa, K., Turon, J., MARGO Project Members, 2009. Constraints on the magnitude and patterns of ocean cooling at the Last Glacial Maximum. Nat. Geosci. 2, 127–132.
Watkins, S., Maher, B., Bigg, G., 2007. Ocean circulation at the Last Glacial Maximum: a combined modeling and magnetic proxy-based study. Paleoceanography 22. http://dx.doi.org/10.1029/2006PA001281.
Watson, A., Bakker, D., Ridgwell, A., Boyd, P., Law, C., 2000. Effect of iron supply on Southern Ocean CO_2 uptake and implications for glacial atmospheric CO_2. Nature 407, 730–733.
Weber, S., Drijfhout, S., Abe-Ouchi, A., Crucifix, M., Eby, M., Ganopolski, A., Murakami, S., Otto-Bliesner, B., Peltier, W., 2007. The modern and glacial overturning circulation in the Atlantic Ocean in PMIP coupled model simulations. Clim. Past 3, 51–64.
Wei, G., Wang, C., Lee, M., Wei, K., 2006. High-resolution benthic foraminifer $\delta^{13}C$ records in the South China Sea during the last 150 ka. Mar. Geol. 232, 227–235.
Wolff, E.W., Fischer, H., Fundel, F., Ruth, U., Twarloh, B., Littot, G.C., Mulvaney1, R., Rothlisberger, R., de Angelis, M., Boutron, C.F., Hansson, M., Jonsell, U., Hutterli, M.A., Lambert, F., Kaufmann, P., Stauffer, B., Stocker, T.F., Steffensen, J.P., Bigler, M., Siggaard-Andersen, M.L., Udisti, R., Becagli, S., Castellano, E., Severi, M., Wagenbach, D., Barbante, C., Gabrielli, P., Gaspari, V., 2006. Southern ocean sea-ice extent, productivity and iron flux over the past eight glacial cycles. Nature 440, 491–496.
Yamanaka, Y., Tajika, E., 1996. The role of the vertical fluxes of particulate organic matter and calcite in the oceanic carbon cycle: studies using an ocean biogeochemical general circulation model. Global Biogeochem. Cycles 10, 361–382.
Yu, E.-F., Francois, R., Bacon, M., 1996. Similar rates of modern and last glacial ocean thermohaline circulation inferred from radiochemical data. Nature 379, 689–694.
Yu, J., Broecker, W., Elderfield, H., Jin, Z., McManus, J., Zhang, F., 2010. Loss of carbon from the deep sea since the Last Glacial Maximum. Science 330, 1084–1087.
Zeebe, R., Marchitto Jr., T.M., 2010. Atmosphere and ocean chemistry. Nat. Geosci. 3, 386–387.
Zeng, N., 2003. Glacial–interglacial atmospheric CO_2 changes – the glacial burial hypothesis. Adv. Atmos. Sci. 20, 677–693.
Zimov, N.S., Zimov, S.A., Zimova, A.E., Zimova, G.M., Chuprynin, V.I., Chapin III, F.S., 2009. Carbon storage in permafrost and soils of the mammoth tundra-steppe biome: role in the global carbon budget. Geophys. Res. Lett. 36. http://dx.doi.org/10.1029/2008GL036332

Commentary of paper

In this paper, Laurie Menviel and others present what is very close to a fully-coupled, 3D ocean carbon cycle model simulation of the Last Glacial cycle demonstrating impressively good agreement with the headline CO_2 and $\delta^{13}C$ records from ice cores. Previous work in this area has generally either been restricted to 2-D ocean models (a massive simplification in the context of the complexity of the dynamical processes involved and the computational demands) or 3D simulations neglecting long-term processes and transients and generally showing very poor agreement with proxy observations. This is therefore an extremely important paper and a substantial advance on previous work. Neil Edwards, The Open University (UK).